ISSN : 2335 - 1357

Mediterranean Journal of Modeling and Simulation

Med. J. Model. Simul. 04 (2015) 001-014

Electromagnetic characterization and modelling of superconducting material

Bruno Douine [a] *, Jean Lévêque [a]

[a] GREEN laboratory - University of Lorraine. BP 239, F-54506 Vandoeuvre les Nancy Cedex

ARTICLE INFO

Article history :
Received June 2015
Accepted July 2015

Keywords :
Superconductor ;
Magnetic field dependence ;
Critical current.

ABSTRACT

Electromagnetic characterization and modelling of superconducting material are very important for end users. Firstly main features of superconducting material are presented. Secondly two methods of characterization to obtain experimentally the influence of magnetic field on critical current density JC are presented. These two methods are commonly used for applications in electrical engineering. The electrical method is based on measuring the voltage and current of a superconducting sample. It has the advantage of simplicity in implementation, but the main drawback as the presence of the self magnetic field. This prevents the determination of the parameters of $J_C(B)$ for weak magnetic fields. The magnetic method using the cycle of magnetization has the advantage of making measurements without contact with the sample but has two drawbacks : it is based on a theoretical model in which J_C is constant and the assumption of infinite length sample.

1. Introduction

The superconducting materials are characterized by three critical quantities that are critical temperature T_C, the critical magnetic field H_C and the critical current density J_C (Wilson, 1983) (Tixador, 1995). The material is superconducting below a critical surface (Figure 1) beyond the material is in normal state. In applications using these superconducting materials, such creation of high magnetic field, magnetic levitation, current transport, motors and transformers, the knowledge of the critical current density J_C of the material is paramount. Thus in the magnetic field coils J_C is related to the maximal magnetic field. In levitation systems J_C sets the power of levitation. In power cable J_C determine AC losses. Finally in electric motors, torque is directly related to J_C. The critical current density is dependent on two other parameters, magnetic field B and temperature T. So the law $J_C(B,T)$ has to be determine. In this article, only $J_C(B)$ determination is exposed. Temperature T is considered constant in superconducting samples.

*Email : bruno.douine@univ-lorraine.fr

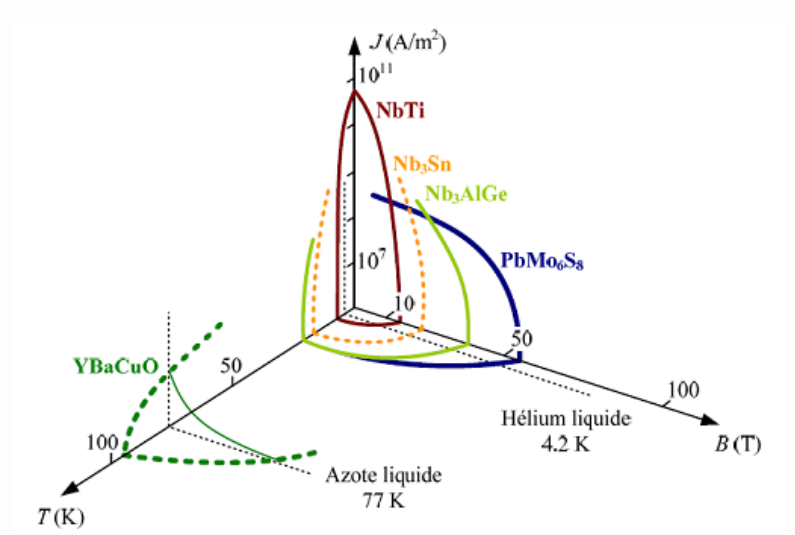

Fig. 1. Critical surface of different superconducting materials

2. Critical magnetic fields

Beyond a critical magnetic field value, the superconductivity disappears. In this regard, two different behaviours define two types of superconductors.

Superconductors of type 1 (Figure 2.a) are characterized by a single critical field H_C. When subjected to an external magnetic field H the magnetic induction B is zero for $H < HC$ and therefore magnetization $M = -H$. Because of their low critical magnetic field, these materials are without interest in electrical engineering.

Type 2 superconductors have two critical field H_{C1} et H_{C2} (Figure 2.b) with $H_{C2} \gg H_{C1}$. They are considered as superconducting state if H is less than H_{C2}. Magnetic induction $\mu_0 \cdot H_{C2}$ is greater than or much greater than the Tesla, so they are more suitable for practical use.

The evolution of the macroscopic magnetic induction B as a function of applied magnetic field H differs from type I between H_{C1} and H_{C2} (Figure 1.2). In this area type II superconductors no longer possesses the property of perfect diamagnetism, screening is partial. It says in a mixed state.

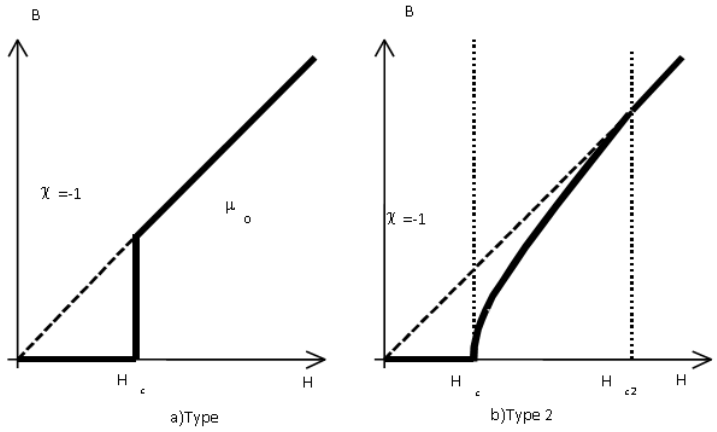

Fig. 2. PV generator monitoring using artificial neural network.

In the mixed state at the microscopic level, there is penetration of magnetic induction in the material as tubes or vortex. They are arranged in triangular lattice Abrikosov or network to minimize the energy of this network. The distance d between the vortices varies with the magnetic induction B :

$$d = k\left[\left(\frac{\varphi_0}{B}\right)^{\frac{1}{2}}\right]$$

Each vortex (Figure 3) has the same quantum of magnetic flux $\varphi_0 = 2,07.10^{-15}Wb$. Its radius is equal to the coherence length ξ. Around these tubes are formed of superconducting shielding currents and the microscopic magnetic induction $B\mu$ decreases exponentially in thickness λ_L. In type II superconductors the coherence length is less than the length of London.

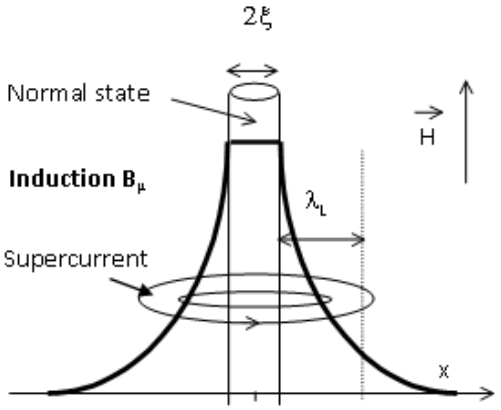

Fig. 3. Vortex structure.

In Figure 4 is represented the case of a superconducting cylinder of type 2 subject to axial magnetic field. Between H_{C1} and H_{C2} the number of vortices increases gradually and eventually occupies the entire material. The magnetic induction B in the material passes so gradually $\mu_0 H_{C1}$ at $\mu_0 H$ (Figure 2).

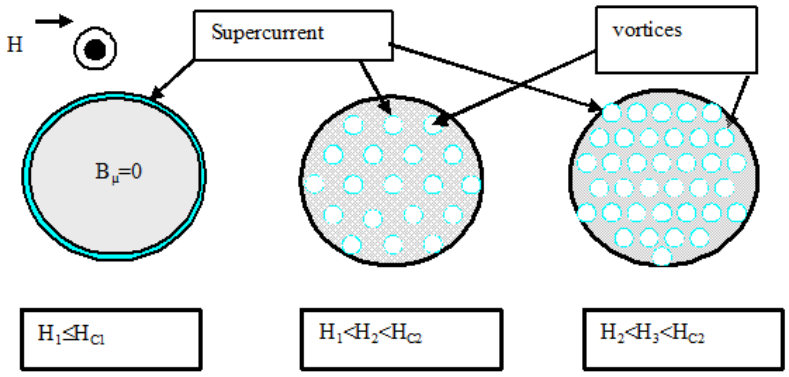

Fig. 4. Increase of B in a type 2 superconducting cylinder between H_{C1} and H_{C2}.

3. E(J) law of superconductor

To remain superconducting state, the current density J in the material must remain below a critical value J_C. This value depends on B and temperature T. The critical current

density J_C is linked to the phenomenon of vortex pinning.

One of the problems of applied superconductivity notation is the definition of different current density. These may be present in the material or measured experimentally. In the first case definitions most commonly used are the following :

J_S is the current density of the supercurrent at the microscopic level that is circulating around the vortex and that is circulating at the surface of the material when $H < H_{C1}$. Its value is about $10^7 A/cm^2$.

J_C is the macroscopic critical current density is related to the local magnetic field H by the macroscopic Maxwell's equation follows :

$$\overrightarrow{rot}\overrightarrow{H} = \overrightarrow{J} = \overrightarrow{J}_C \tag{1}$$

In case of high critical temperature superconductors, materials that are anisotropic, J_C is in several different values for different directions.

Values of critical currents are obtained experimentally or by an electrical method (J_{CT}) or by a magnetic method (J_{CM}). In the first case transport current traverses the sample. In the second case superconducting sample is subjected to a magnetic field.

The difficulty is obviously to move from the measured quantity to the real quantity in the material.

Superconductors of type 2, in which there are vortices, cannot carry current without dissipating. If there is a current in a superconductor with a direction perpendicular to the external magnetic field which creates the vortex, it produces two phenomena (figure 5).

First the self magnetic field created by the transport current creates an imbalance between an area of strong magnetic field on one side of the superconductor and a low field region to the other side.

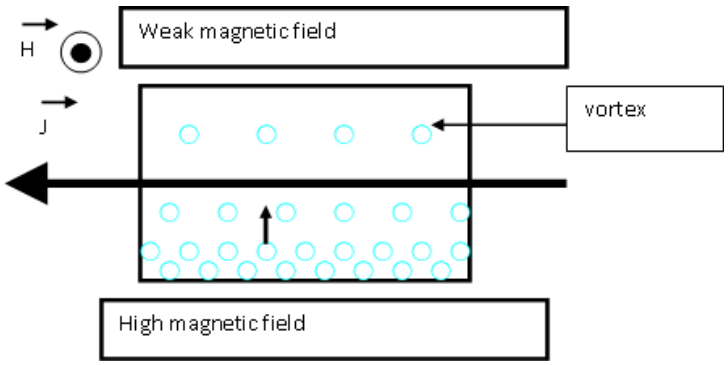

Fig. 5. Moving vortex in a superconducting material traversed by an transport current perpendicular to the direction of the vortex.

On the other hand, the vortices are subjected to a Lorentz force if the current direction is different from the applied external field direction :

$$\overrightarrow{F}_L = \overrightarrow{J} \wedge \overrightarrow{B} \tag{2}$$

The vortices will move from a region of strong magnetic field to a region of low field where they disappear, generating an electric field and therefore energy dissipation. This results in a resistivity ρ_f dependent of B and resistivity in the normal state ρ_n :

$$\rho_f = \left(\frac{B}{B_{C2}}\right)\rho_n \tag{3}$$

The curve $B(H)$ of type 2 superconductors (Figure 2) is actually a curve that exists only in the case of a perfect crystal of superconductor, without defects and impurities. If you submit this material to a magnetic field H the vortices are distributed uniformly in the section perpendicular to H as shown in Figure 4. This therefore produces a macroscopic magnetic induction B uniform in this section. This is not the case most of the time in the materials used in reality. In these materials the defects (dislocations, impurities, grain boundaries etc.) will block the vortex at pinning sites. In this case if the material is subjected to a magnetic field (Figure 4), the distribution of vortices in the cylinder is different from the previous case (Figure 6). If H is less than or equal to H_{C1} there is no difference because there is not vortex. If H is greater than H_{C1} and lower than H_{C2} vortices first appear on the outer surface or they are trapped. This results in the presence of two distinct zones. A first outer zone with presence of vortices where B is different from zero and an inner zone without vortex where B is zero. This spatial variation of B creates current densities induced in the superconducting material. C.P. Bean has shown that these induced currents have a current density equal to the critical current density J_C. That is the critical state model of Bean.

Between H_{C1} and H_{C2} is defined the full penetration magnetic field H_P for which the vortices and the current density fully penetrate the material. Beyond H_P the number of vortices and therefore B increases to B_{C2}. The current density still exists in this case throughout the material but decreases when B increases until zero at $H = H_{C2}$.

To obtain high J_C materials is important to have the largest number of defects. This property of materials with trapping sites contain large volume flows, has led to the development of applications such as magnetic field shielding and trapping of magnetic flux for the realization of superconducting magnets.

In practical, type 2 superconductors are used only with pinning sites and therefore we refer only to them later in this article.

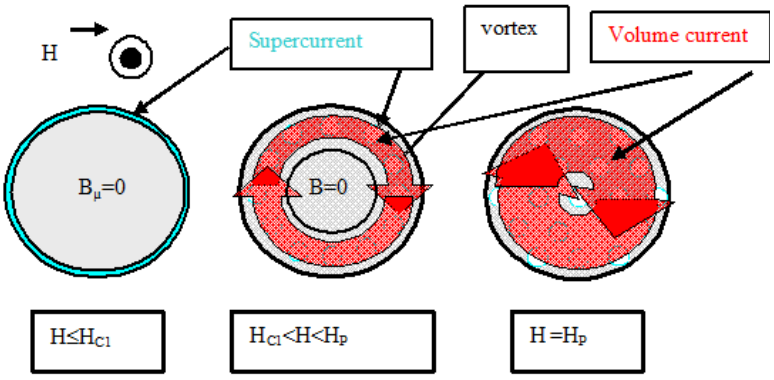

Fig. 6. Increase of B for H between H_{C1} and H_{C2} in a type 2 superconducting cylinder with pinning.

In a non-superconducting conductive material relationship between the electric field E and current density is $E = \rho \cdot J$. The characteristic $E(J)$ of a superconductor is very

different and varies depending on temperature and magnetic field. In this section we consider a superconducting material in which these vortices are created by an external field and a current transmission direction perpendicular to the direction of the vortices. These vortices are therefore subject to the Lorentz force defined above.

In Figure 7 the characteristic $E(J)$ of a superconductor at very low temperatures is shown. For small values of J less than J_C, the vortices are embedded as the Lorentz force is less than the pinning force and in this case $E = 0$. The critical current density is one for which the Lorentz force F_L is greater than the pinning force F_P causing a shift to the state of "flux flow". In this case the vortices move together and the losses are equivalent to those due to viscous friction. The critical current density is one that will untie the vortex from defects causing a transition to the state of "flux flow". The growth of E is very large when $J > J_C$ and thus the material passes very quickly to the normal state when J increases. We can therefore consider that if the material is superconducting and $J = J_C$, this is the critical state model of Bean.

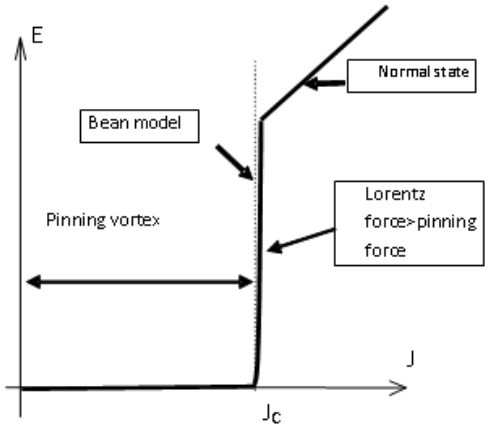

Fig. 7. $E(J)$ law of superconductor at very low temperature.

In Figure 8 the characteristic $E(J)$ of a superconductor at temperatures where the influence of thermal effects is important is shown. The thermal motion makes it likely that the movement of vortices even if $F_L < F_A$ and helps to round off the characteristic $E(J)$ (Figure 8). For low values of E with J close to the J_C curve $E(J)$ is of exponential form, is the region of “flux-creep”. This corresponds to displacement of the vortices due to thermal activation and thus the appearance of a weak electric field but nonzero. For high values of E with $J > J_C$ is the region of flux flow. In practice the operating temperature in applications that use superconducting materials is usually high enough that it can be seen in the latter case. It is obvious that in the case of high critical temperature superconductors used relatively high temperatures these phenomena related to the thermal motion become dominant. The critical current density is the value for which the material passes from the state of “flux creep” in the state of “flux flow”. The transition between these two states is gradual and therefore difficult to identify experimentally. To define J_C in this case we use a critical electric field criterion ($0.1\mu V/cm$ or $1\mu V/cm$ for example) that do not necessarily correspond to the physical border between two states but is a convenient practical criterion for comparing performance of different superconducting materials.

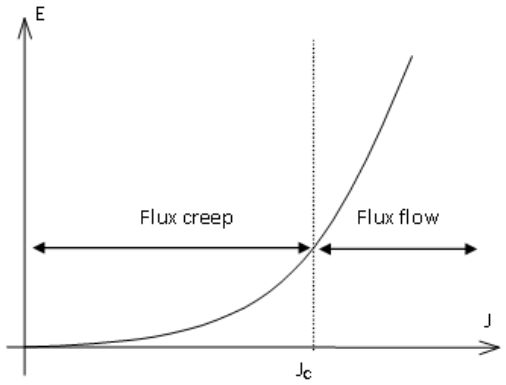

Fig. 8. $E(J)$ law of superconductor at "hot" temperature.

4. $J_C(B)$ laws of superconductor

In superconductor the relation between J and J is :

$$\vec{E} = E_C.\left(\frac{J}{J_C(B,T)}\right)^{n(B,T)}.\frac{\vec{J}}{J} \tag{4}$$

For LTS, n is large (several tens). But for HTS n varies between 7 and 30. The value of n is determined from experimental curves. If n tends to infinity the relation $E(J)$ is equal to the critical state model developed by Bean (Bean, 1964). This requires that the local density of current in a superconducting material is either zero or equal to its critical value J_C.

$$J = \pm J_C \; ou \;\; J = 0 \tag{5}$$

In [4], the critical current density is defined for a criterion of critical electric field $EC(0.1, 1$ or $10\mu V/cm)$. For HTS, n is relatively small and the critical current varies enormously depending on the test. E_C value most used for HTS is $1\mu V/cm$.

The most commonly used $J_C(B)$ relationships in literature are (Table 1) models of Bean (Bean, 1964), Kim (Kim, 1962) and linear (Watson, 1968) (Douine et al., 2006) . The Bean model is widely used in theoretical calculations because it allows simple analytical calculations of current distribution in a superconducting material such as a plate or cylinder. The linear model is valid especially for LTS and allows analytic calculations of losses (Douine et al., 2008). The model of Kim is valid for granular first-generation HTS, where the flow of transport current is a intergranular current.

Table 1. $J_C(B)$ law.

$J_{CB} = J_{c0}$ independent of B	Bean (6)
$J_{CK}(B) = \frac{J_{C0}}{\left(1+\frac{\lvert B\rvert}{B_{K0}}\right)}$	Kim (7)
$J_{CL}(B) = \frac{J_{C0}(B_{j0}-\lvert B\rvert)}{B_{j0}}$	Linear (8)

J_{C0}, B_{K0} and B_{j0} are positive constants.

5. DC characterization of superconductors

$J_C(B)$ law of a superconducting material can be obtained in several ways (Vanderbemden, 1999) (Senoussi, 1992). This paper will be presented an electrical method, where the sample is in contact with the measuring system it is called direct method, and a magnetic method, where the sample is not in contact with the system of measurement, referred to as indirect method.

5.1. $J_C(B)$ determination electric method

Electrical measurements of critical current density of superconducting materials are usually performed by the 4-point method (Douine et al., 2006) (Senoussi, 1992). The sample is fed by a current I and a voltage U across the sample is measured by two wires (Figure 9). So simple even simplistic E is deduced from U by $U = EL$ with L the distance between the voltage taps and J is deduced from I by $J = J/S$ with S section of the sample. These relationships are theoretically valid only if the current density has fully penetrated the sample and so the current is large enough. However these relationship are generally used also low current. In addition for high currents, thermal effects due to losses in the superconducting material and contact resistances above-copper prevented making perfectly isotherm measurements. J_C is deduced from $E(J)$ with an electric field criterion equal $1\mu V/cm$. To obtain experimental $J_C(B)$ curve (Figure 10), the sample supplied with a current I is subjected to an external magnetic field B_{ext} parallel to its axis. The voltage U is measured as a function of I for different external magnetic fields (Figure 11). To differentiate the local $J_C(B)$ in material and $J_C(B)$ deduced from measurements, this last one is noted $J_{mc}(B_{ext})$ thereafter.

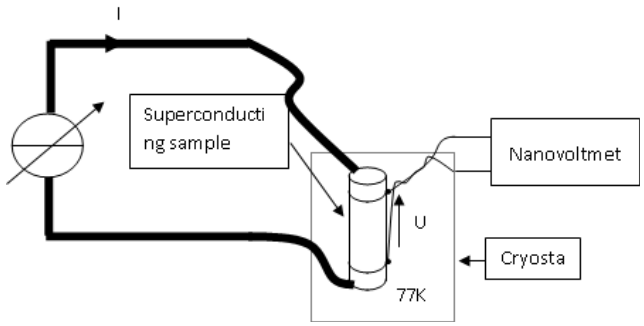

Fig. 9. 4-points electric method.

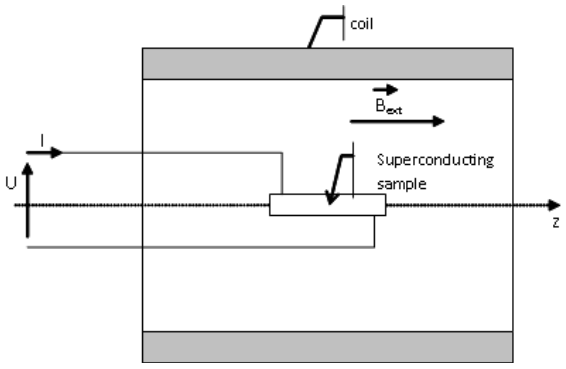

Fig. 10. Experimental bench for $J_C(B)$ electric determination.

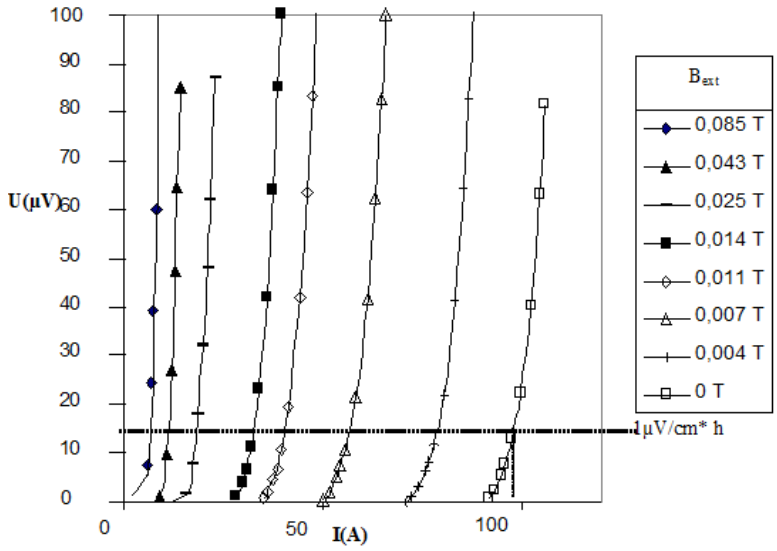

Fig. 11. $U(I)$ curves for different B_{ext}.

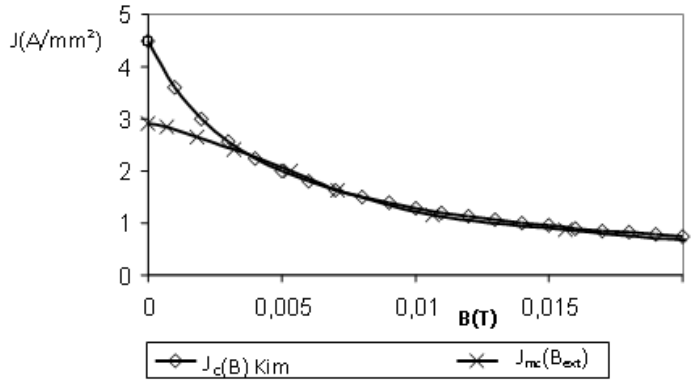

Fig. 12. Experimental $J_{mc}(B_{ext})$ curve and Kim model curve.

Measurements are made (figure 11 and 12) for superconducting tube (internal radius $Ri = 3.8mm$, external radius $Re = 5mm$, section $S = 33mm^2$, distance between electric taps $h = 11.7cm$). For no applied magnetic field, measured critical current $I_{mc0} = 96A$, ($1\mu V/cm$ criteria).

The electrical method is relatively simple to implement but requires a good knowledge of physical phenomena (thermal problems, self-field) involved in the material during measurement.

5.2. $J_C(B)$ determination magnetic method

The electrical method or direct method requires connection of the superconducting sample to a current source. This introduces problems because of the thermal energy input important at low temperature. To avoid this problem methods without electrical connections called indirect methods or magnetic methods exist. They are of two types, DC and AC method. The latter is not described in this article but the reader may find it in a number of references (Vanderbemden, 1999) (Senoussi, 1992). The principle of the

DC method is as follows. The superconducting sample is subjected to an applied magnetic field H_a which causes the onset of screening currents induced in the sample (Figure 13). These induced currents create a magnetic moment m which is likened to a magnetization ($M = m/V$; V is the volume of superconducting material). The local magnetic field H is the vector sum of the applied magnetic field and induced field H_i created by the supercurrent :

$$\overrightarrow{H} = \overrightarrow{H_a} + \overrightarrow{H_i} \tag{9}$$

Average magnetic induction $< B >$ is the sum of applied magnetic field and M :

$$< B >= \mu_0 H_a + \mu_0 M \tag{10}$$

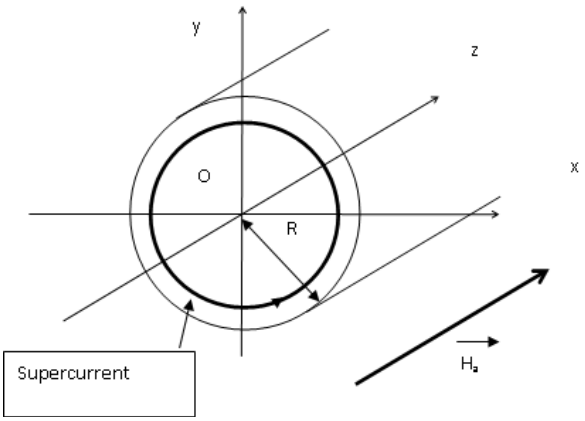

Fig. 13. Superconducting cylinder in applied magnetic field.

To obtain M experimentally the method is as follows. The superconducting sample is placed at the end of a rod connected to a linear motor and in a region subjected to an applied field H_a almost uniform (Figure 14). The measurement is done in two phases (Figure 15). First phase a magnetic field is applied gradually. Second phase, the magnetic field is held constant and the sample is moved upwards. An induced voltage $e(t)$ due to the supercurrent induced in the material is recorded by the measuring system. The curve $M(H_a)$ is deduced (Figure 16) using the following formula

$$M = \frac{< B >}{\mu_0} - H_a = -\frac{\phi_{\max}}{S.\mu_0} - H_a = \frac{\int e(t).dt}{S.\mu_0} - H_a \tag{11}$$

The curve $M(H_a)$ consists of two parts. First, an initial magnetization curve $M_1(Ha)$. It begins as the superconducting material contains no current and ends for $H_a = H_{max}$. Second, a hysteresis loop for H_a from H_{max} to $-H_{max}$.

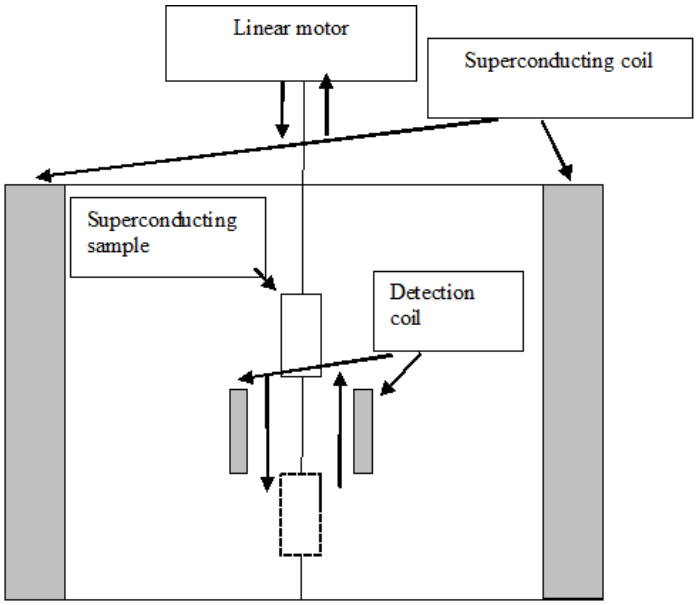

Fig. 14. $M(H_a)$ experimental bench.

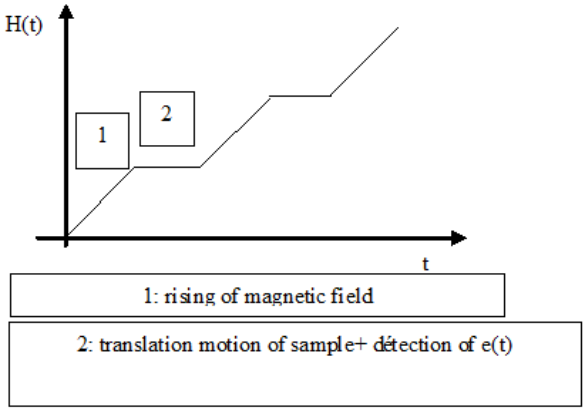

Fig. 15. $M(H_a)$ determination method.

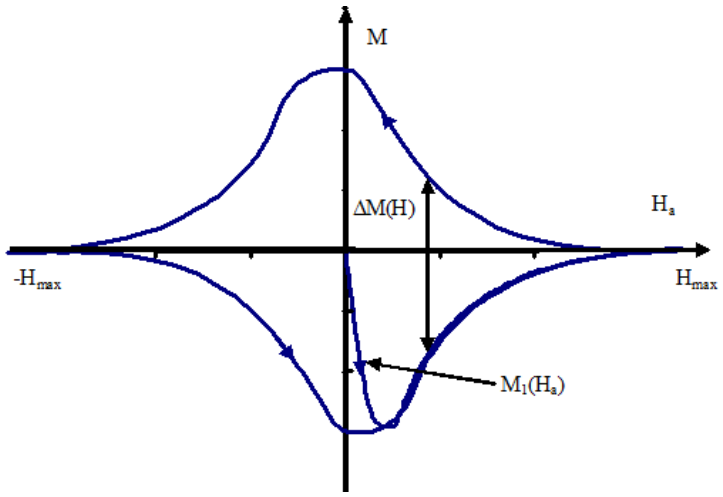

Fig. 16. Measured $M(H_a)$ of superconducting sample.

Currently the most widely used model to deduce $J_C(B)$ from $M(H_a)$ is the critical state model. Bean model (Table 1) is a $J_C(B)$ relationship where J_C is constant. The model of the critical state requires a simple relationship between J_C and H

$$\overrightarrow{rot}\overrightarrow{H} = \overrightarrow{J}_C \tag{12}$$

In the case of a superconducting sample subjected to an axial field the relationship between B and J_C is then (Tixador, 1995) :

$$\frac{dB}{dr} = \mu_0 J_C \tag{13}$$

The distributions of $B(r)$ and $J(r)$ (Figure 17) are deduced from [13]. During the first increase of the applied magnetic field, there is firstly, incomplete penetration of the magnetic field in the cylinder and secondly from the full penetration magnetic field H_{PB} magnetic field is present everywhere in the material and also$J = J_C$ everywhere. H_{PB} is deduced using [13] :

$$H_{PB} = R.J_C \tag{14}$$

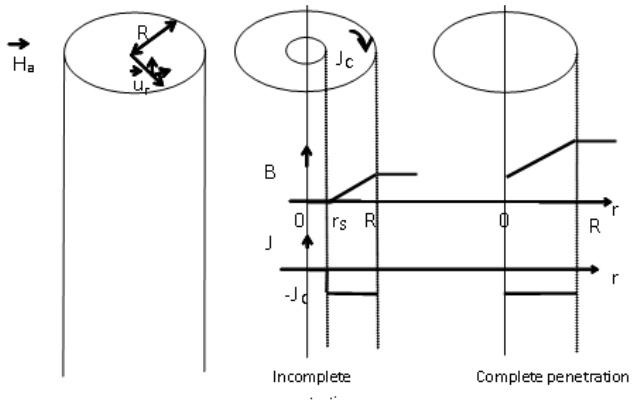

Fig. 17. $B(r)$ and $J(r)$ distribution during first magnetization of superconducting cylinder.

Equation [13] allows calculating the theoretical curve $M(H_a)$ (Figure 1.21). As the experimental curve, it consists of an initial magnetization curve $M_{1B}(H_a)$ and a hysteresis loop. The theoretical curve of first magnetization is also decomposed into two parts. Below H_{PB} there is incomplete penetration of the magnetic field in the sample (subscript I), above H_{PB} there is complete penetration (subscript C) :

$$M_{1BI}(H_a) = -\frac{H_a\left((\mu_0 H_a)^2 - \mu_0^2 H_a.J_{C0}R + 3(\mu_0 J_{C0}R)^2\right)}{3(\mu_0 J_{C0}R)^2} \tag{15}$$

$$M_{1BC}(H_a) = -\frac{J_{C0}R}{3} = -\frac{H_{PB}}{3} \tag{16}$$

There is a simple relationship between the cycle depth ΔM and J_C :

$$J_C = J_{C0} = \frac{3\Delta M}{2R} \tag{17}$$

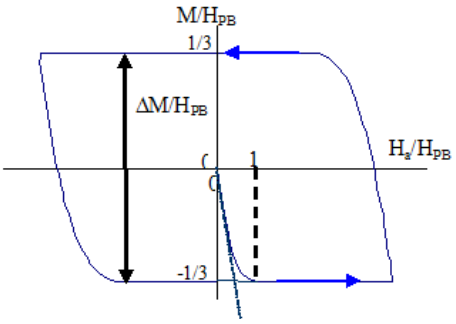

Fig. 18. Bean model theoretical $M(H_a)$ cycle.

The traditional method of determination of $J_C(B)$ (Vanderbemden, 1999) (Senoussi, 1992) (Chen et al., 1989) using the cycle $M(H_a)$ is therefore used [17], calculated using the J_C Bean model which is constant in the extrapolation to cases where J_C is dependant of B :

$$J_C(B) = \frac{3\Delta M(H)}{2R} \tag{18}$$

In Figure 19 is represented the $J_C(B)$ curve of the material which the curve $M(H_a)$ is shown in Figure 16. This is a NbTi cylinder, $2cm$ long and $5mm$ diameter at a temperature of $5°K$. On the same figure is represented the law $J_C(B)$ deduced from Kim model and that is closest to the experimental measurement (Douine et al., 2010).

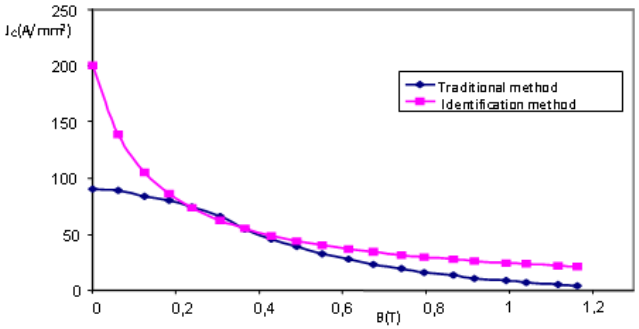

Fig. 19. $J_C(B)$ curves deduced from $M(H)$ measurement and calculated with Bean model and with identification method.

6. Conclusion

Knowledge of the law $J_C(B)$ of a superconducting material is very important for users. In this article two methods of characterization to obtain experimentally the law $J_C(B)$

are presented. These two methods are commonly used for applications in electrical engineering. The electrical method is based on measuring the voltage and current of a superconducting sample. It has the advantage of simplicity in implementation, but the main drawback as the presence of the magnetic field clean. This prevents the determination of the parameters of $J_C(B)$ for weak magnetic fields. The magnetic method using the cycle of magnetization has the advantage of making measurements without contact with the sample but has two drawbacks : it is based on a theoretical model in which J_C is constant and the assumption of infinite length sample.

REFERENCES

[1] Bean C. P., « Magnetization of high field superconductors », Review of modern physics, 1964, p. 31-39.
[2] Douine B., Berger K., Leveque J., Netter D. Rezzoug A., «Influence of Jc(B) on the full penetration current of superconducting tube» Physica C, vol. 443, pp. 23-28, 2006.
[3] Douine B., Berger K., Pienkos J., Leveque J., Netter D., Analytical calculation of the instantaneous power in a current carrying superconducting tube with Jc(B), I.E.E.E. transactions on applied superconductivity, 18(3), pp.1717-1723, september 2008.
[4] Douine B., Leveque J., Mezani S., JC(B) determination method with the help of the virgin magnetization curve of a superconducting cylinder, I.E.E.E. transactions on applied superconductivity, vol. 20(2), pp.82-86,.2010.
[5] Kim Y. B., Hempstead C. F., Strnad A. R., «Critical persistent currents in hard superconductors», Phys. Rev. Lett., volume n°9, 1962, pp. 306-309.
[6] Senoussi S., «Review of the critical current densities and magnetic irreversibilities in high Tc superconductors», Journal de physique III, Vol. 2, 1992, pp. 1041-1257.
[7] Tixador P., Les supraconducteurs, Paris, Hermès, 1995.
[8] Vanderbemden P., «Determination of critical current in bulk high temperature superconductors by magnetic flux profile measuring methods», Ph. D. Thesis, U. Lg. (1999), 193 p.
[9] Watson J. H. P., «Magnetization of Synthetic Filamentary Superconductors, the dependence of the critical current density on temperature and magnetic field», J. Appl. Phys., vol.39, n°7, juin 1968, pp.3406-3413.
[10] Wilson M. N., Superconducting Magnets, Oxford science publications, 1983.

ISSN : 2335 - 1357

Mediterranean Journal of Modeling and Simulation

Med. J. Model. Simul. 04 (2015) 015-036

Product of likelihood ratio scores fusion of dynamic face, text independent speech and on-line signature based biometrics verification application systems

Mohamed Soltane [a] *,

[a] Electrical Engineering & Computing Department, Faculty of Sciences & Technology, Doctor Yahia Fares University of Medea, 26000 Medea, Algeria. Laboratoire des Systèmes Électroniques Avancées (LSEA)

ARTICLE INFO

Article history :
Received June 2015
Accepted August 2015

Keywords :
Biometry ;
Multi-Modal ;
Authentication ;
Face Recognition ;
Speaker and Signature Verification ;
Data Fusion ;
Adaptive Bayesian decision ;
GMM ;
EM ;
Likelihood Ratio.

ABSTRACT

In this paper, the use of finite Gaussian mixture modal (GMM) tuned using Expectation Maximization (EM) estimating algorithms for score level data fusion is proposed. Automated biometric systems for human identification measure a "signature" of the human body, compare the resulting characteristic to a database, and render an application dependent decision. These biometric systems for personal authentication and identification are based upon physiological or behavioral features which are typically distinctive, Multi-biometric systems, which consolidate information from multiple biometric sources, are gaining popularity because they are able to overcome limitations such as non-universality, noisy sensor data, large intra-user variations and susceptibility to spoof attacks that are commonly encountered in mono modal biometric systems. Simulation result show that finite mixture modal (GMM) is quite effective in modelling the genuine and impostor score densities, fusion based the product of Likelihood Ratio achieves a significant performance on eNTERFACE 2005 multi-biometric database based on dynamic face, on-line signature and text independent speech modalities.

1. Introduction

BIOMETRIC is a Greek composite word stemming from the synthesis of bio and metric, meaning life measurement. In this context, the science of biometrics is concerned with the accurate measurement of unique biological characteristics of an individual in order to securely identify them to a computer or other electronic system. Biological characteristics measured usually include fingerprints, voice patterns, retinal and iris scans, face patterns, and even the chemical composition of an individual's DNA [1]. Biometrics authentication (BA) (*Am I whom I claim I am ?*) involves confirming or denying a person's *claimed*

*Email : soltane.mohamed.3099@gmail.com

identity based on his/her physiological or behavioral characteristics [2]. BA is becoming an important alternative to traditional authentication methods such as keys ("something one has", i.e., by possession) or PIN numbers ("something one knows", i.e., by knowledge) because it is essentially "who one is", i.e., by biometric information. Therefore, it is not susceptible to misplacement or forgetfulness [3].

Some works based on multi-modal biometric identity verification systems has been reported in literature. Ben-Yacoub et al. [4] evaluated five binary classifiers on combinations of face and voice modalities (XM2VTS database). They found that (i) a support vector machine and bayesian classifier achieved almost the same performances ; and (ii) both outperformed Fisher's linear discriminent, a C4.5 decision tree, and a multilayer perceptron. Korves et al.[5] compared various parametric techniques on the BSSR1 dataset. That study showed that the Best Linear technique performed consistently well, in sharp contrast to many alternative parametric techniques, including simple sum of z-scores, Fisher's linear discriminant analysis, and an implementation of sum of probabilities based on a normal (Gaussian) assumption. Jain et al. [6] propose a framework for optimal combination of match scores that is based on the likelihood ratio test. The distributions of genuine and impostor match scores are modeled as finite Gaussian mixture model. The proposed fusion approach is general in its ability to handle (i) discrete values in biometric match score distributions, (ii) arbitrary scales and distributions of match scores, (iii) correlation between the scores of multiple matchers and (iv) sample quality of multiple biometric sources. The performance of complete likelihood ratio based fusion rule was evaluated on the three partitions of the NIST-BSSR1 database and the XM2VTS-Benchmark database. As expected, likelihood ratio based fusion leads to significant improvement in the performance compared to the best single modality on all the four databases. Jain et al. [7] applied the sum of scores, max-score, and min-score fusion methods to normalized scores of face, fingerprint and hand geometry biometrics (database of 100 users, based on a fixed TAR). The normalized scores were obtained by using one of the following techniques : simple distance-to-similarity transformation with no change in scale (STrans), min–max, z-score, median-MAD, double sigmoid, tanh, and Parzen. They found that (a) the min–max, z-score, and tanh normalization schemes followed by a simple sum of scores outperformed other methods ; (b) tanh is better than min-max and z-score when densities are unknown ; and (c) optimizing the weighting of each biometric on a user-by-user basis outperforms generic weightings of biometrics. Kittler et al. [8] proposed a multi-modal person verification system, using three experts : frontal face, face profile, and voice. The best combination results are obtained for a simple sum rule. Snelick et al. [9] compared combinations of z-score, min-max, tanh and adaptive (two-quadrics, logistic and quadric-line-quadric) normalization methods and simple sum, min score, max score, matcher weighting, and user weighting fusion methods (database of about 1000 users, at a fixed FAR). They found that (a) fusing COTS fingerprint and face biometrics does outperform mono-modal COTS systems, but the high performance of mono-modal COTS systems limits the magnitude of the performance gain ; (b) for open-population applications (e.g., airports) with unknown posterior densities, min-max normalization and simple-sum fusion are effective ; (c) for closed-population applications (e.g. an office), where repeated user samples and their statistics can be accumulated, QLQ adaptive normalization and user weighting fusion methods are effective. Teoh et al. [10]

Applied a modified k-NN and evidence theoretic k-NN classifier based on Dampster-safer theory, and it found that the best result is obtained using the evidence theoretic k-NN classifier as it introduces low FAR and FRR compared to both the ordinary and modified k-NN. Youssef Elmir et al. [11] present a hierarchical strategy fusion based on multimodal biometric system. The strategy presented relies on a combination of several biometric traits using a multi-level biometric fusion hierarchy. The multi-level biometric fusion includes a pre-classification fusion with optimal feature selection and a post-classification fusion that is based on the similarity of the maximum of matching scores. Mandeep Kaur et al. [12] discusses about Multimodal Biometric System such as signature and speech modalities which are used to overcome some of the problems of uni-modal systems like noise in sensed data, intra-class variations, distinctiveness, and spoof attacks.

A multi-modal biometric verification system based on still facial, on-line signature and text independent vocal modalities is described in this paper. All dynamics face images, signatures and speech biometrics are chosen due to their complementary characteristics, physiology, and behavior. In multimodal systems, complementary input modalities provide the system with non-redundant information whereas redundant input modalities allow increasing both the accuracy of the fused information by reducing overall uncertainty and the reliability of the system in case of noisy information from a single modality. Information in one modality may be used to disambiguate information in the other ones. The enhancement of precision and reliability is the potential result of integrating modalities and/or measurements sensed by multiple sensors [13].

2. Authentication Traits

2.1. Face Extraction and Recognition

Face recognition, authentication and identification are often confused. Face recognition is a general topic that includes both face identification and face authentication (also called verification). On one hand, face authentication is concerned with validating a claimed identity based on the image of a face, and either accepting or rejecting the identity claim (one-to-one matching). On the other hand, the goal of face identification is to identify a person based on the image of a face. This face image has to be compared with all the registered persons (one-to-many matching). Thus, the key issue in face recognition is to extract the meaningful features that characterize a human face. Hence there are two major tasks for that : Face detection and face verification.

2.1.1. Face detection

Face detection is concerned with finding whether or not there are any faces in a given image (usually in gray scale) and, if present, returns the image location and content of each face. This is the first step of any fully automatic system that analyzes the information contained in faces (e.g., identity, gender, expression, age, race and pose). While earlier work dealt mainly with upright frontal faces, several systems have been developed that are able to detect faces fairly accurately with in-plane or out-of-plane rotations in real time. For biometric systems that use faces as non-intrusive input modules, it is imperative to locate faces in a scene before any recognition algorithm can be applied. An intelligent vision based user interface should be able to tell the attention focus of the user (i.e., where the user is looking at) in order to respond accordingly. To detect facial features accurately

for applications such as digital cosmetics, faces need to be located and registered first to facilitate further processing. It is evident that face detection plays an important and critical role for the success of any face processing systems.

On the results presented on this paper only size normalization of the extracted faces was used. All face images were resized to 130x150 pixels, applying a bi-cubic interpolation. After this stage, it is also developed a position correction algorithm based on detecting the eyes into the face and applying a rotation and resize to align the eyes of all pictures in the same coordinates. The face detection and segmentation tasks presented in this paper was performed based on 'Face analysis in Polar Frequency Domain' proposed by Yossi Z. et al. [14]. First it extract the Fourier-Bessel (FB) coefficients from the images. Next, it computes the Cartesian distance between all the Fourier-Bessel transformation (FBT) representations and re-define each object by its distance to all other objects. Images were transformed by a FBT up to the 30^{th} Bessel order and 6^{th} root with angular resolution of 3°, thus obtaining to 372 coefficients. These coefficients correspond to a frequency range of up to 30 and 3 cycles/image of angular and radial frequency, respectively. Figure 1. Shows the face and eyes detections for different users from the database, and figure 2. Shows the face normalization for the same users.

Fig. 1. Face & Eyes Detections for different users..

Fig. 2. Face Normalization for the above users.

Polar Frequency Analysis : The FB series is useful to describe the radial and angular components in images [14]. FBT analysis starts by converting the coordinates of a region of interest from Cartesian (x, y) to polar (r, θ). The f (r, θ) function is represented by the two-dimensional FB series, defined as :

$$f(r,\theta)=\sum_{i=1}^{\infty}\sum_{n=1}^{\infty}A_{n,i}J_n(\alpha_{n,i}r)\cos(n\theta)+\sum_{i=1}^{\infty}\sum_{n=1}^{\infty}B_{n,i}J_n(\alpha_{n,i}r)\sin(n\theta) \quad (1)$$

where J_n is the Bessel function of order n, $f(R,\theta)=0$ and $0\leq r\leq R$. $\alpha_{n,i}$ is the ith root of the J_n function, i.e. the zero crossing value satisfying $J_n(\alpha_{n,i})=0$ is the radial distance to the edge of the image. The orthogonal coefficients $A_{n,i}$ and $B_{n,i}$ are given by :

$$A_{0,i}=\frac{1}{\pi R^2 J_1^2(\alpha_{n,i})}\int_{\theta=0}^{\theta=2\pi r=R}\int_{r=0}f(r,\theta)\,rJ_n\left(\frac{\alpha_{n,i}}{R}r\right)drd\theta \quad (2)$$

if $B_{0,i}=0$ and $n=0$;

$$\begin{matrix}A_{n,i}\\B_{n,i}\end{matrix}=\frac{2}{\pi R^2 J_{n+1}^2(\alpha_{n,i})}\int_{\theta=0}^{\theta=2\pi r=R}\int_{r=0}f(r,\theta)\,rJ_n\left(\frac{\alpha_{n,i}}{R}r\right)\begin{matrix}\cos(n\theta)\\\sin(n\theta)\end{matrix}drd\theta \quad (3)$$

if $n>0$.

An alternative method to polar frequency analysis is to represent images by polar Fourier transform descriptors. The polar Fourier transform is a well-known mathematical operation where, after converting the image coordinates from Cartesian to polar, as described above ; a conventional Fourier transformation is applied. These descriptors are directly related to radial and angular components, but are not identical to the coefficients extracted by the FBT.

2.1.2. Face Verification

Feature Extraction : The so-called "Eigen faces" method [15] is one of the most popular methods for face recognition. It is based on the Principal Components Analysis (PCA) of the face images in a training set. The main idea is that since all human faces share certain common characteristics, pixels in a set of face images will be highly correlated. The K-L (Karhunen-Loeve) transform can be used to project face images to a different vector space that is of reduced dimensionality where features will be uncorrelated. In the new space nearest neighbor classifiers can be used for classification. Euclidean distances d in the projection space are mapped into the [0,1] interval of the real line using the mapping function : $f=d/(1+d)$. It is easily seen that f is also a metric with distance values in [0,1]. Thus, the decomposition of a face image into an Eigen face space provides a set of features. The maximum number of features is restricted to the number of images used to compute the KL transform, although usually only the more relevant features are selected, removing the ones associated with the smallest eigenvalues. And it's used for the following processing stages, database training stage and the operational stage [15]. The concept verification system is illustrated in figure 4.

The training stage : Face spaces are eigenvectors of the covariance matrix corresponding to the original face images, and since they are face-like in appearance, they are so called Eigen faces.

Consider the training set of face images be i_1, $i_2, \cdots$, i_m ; the average face of the set is defined as :

$$\bar{\imath} = \frac{1}{M} \sum_{j=1}^{M} i_j \tag{4}$$

Where M is the total number of images.

Each face differs from the average by the vector $\phi_n = i_n - \bar{\imath}$. A covariance matrix is constructed where :

$$C = \sum_{j=1}^{M} \phi_j \phi_j^T = AA^T \tag{5}$$

Where

$$A = [\phi_1 \phi_2 \cdots \phi_M]$$

Then, the eigenvectors v_k and the eigenvalues λ_k with a symmetric matrix C are calculated. v_k Determines the linear combination of M difference images with ϕ to form the Eigen faces :

$$u_l = \sum_{k=1}^{M} v_{lk} \emptyset_k l = 1, \ldots, M \tag{6}$$

From these Eigen faces, $K(< M)$ Eigenfaces are selected corresponding to the K highest eigenvalues.

At the training stage, a set of normalized face images, $\{i\}$, that best describe the distribution of the raining facial images in a lower dimensional subspace (Eigen face) is computed by the following operation :

$$\omega_k = u_k \left(i_n - \bar{\imath}\right) \tag{7}$$

Where $n = 1, \cdots, M$ and $k = 1, \cdots, K$.

After that, the training facial images are projected onto the Eigen space, $\mathbf{\Omega}_i$, to generate representations of the facial images in Eigenface :

$$\mathbf{\Omega}_i = (\omega_{n1}, \omega_{n2}, \ldots, \omega_{nk}) \tag{8}$$

Where $n = 1, \cdots, M$.

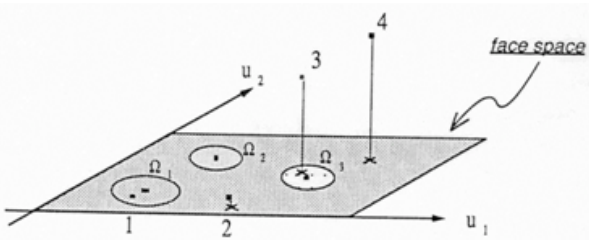

Fig. 3. Simplified version of the face space illustrating the four results of the projection of an image onto the face space. In this case there are two Eigen faces, u_1 and u_2 [15].

The operational stage : This approach is based on the same principles as standard PCA, explained in the training stage. The difference is that an Eigen face space is extracted for each user. Thus, when a claimant wants to verify its identity, its vectorized face image is projected exclusively into the claimed user Eigen face space and the corresponding likelihood is computed. The advantage of this approach is that it allows a more accurate model of the user's most relevant information, where the first Eigen faces are directly the most representative user's face information. Another interesting point of this method is its scalability in terms of the number of users. Adding a new user or new pictures of an already registered user only requires computing or recomputed the specific Eigen face space, but not the whole dataset base as in the standard approach. For verification systems, the computation of the claimant's likelihood to be a specific user is independent on the number of users in the dataset. On the contrary, for identification systems, the number of operations increases in a proportional way with the number of users, because as many projections as different users are required. In the verification system described in this article, the independent user Eigen face approach has been chosen. Each user's Eigen face space was computed which 16 frames extracted from the database still faces.

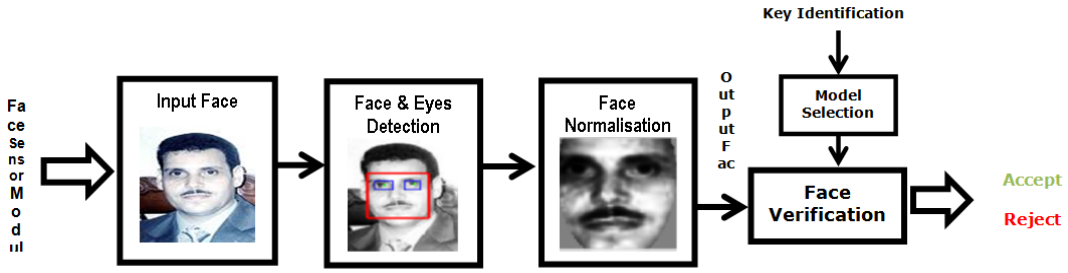

Fig. 4. Face Verification Concept System.

2.2. Face Verification Concept System.

Gaussian Mixture Models (GMMs), is the main tool used in text-independent speaker verification, in which can be trained using the Expectation Maximization (EM) algorithm [16][17]. In this work the speech modality, is authenticated with a multi-lingual text-independent speaker verification system. The speech trait is comprised of two main components as shown in figure 5 : speech feature extraction and a Gaussian Mixture Model (GMM) classifier. The speech signal is analyzed on a frame by frame basis, with a typical frame length of 20 ms and a frame advance of 10 ms [18]. For each frame, a dimensional feature vector is extracted, the discrete Fourier spectrum is obtained via a fast Fourier transform from which magnitude squared spectrum is computed and put it

through a bank of filters. The critical band warping is done following an approximation to the Mel-frequency scale which is linear up to 1000 Hz and logarithmic above 1000 Hz. The Mel-scale cepstral coefficients are computed from the outputs of the filter bank [19]. The state of the art speech feature extraction schemes (Mel frequecy cepstral coefficients (MFCC) is based on auditory processing on the spectrum of speech signal and cepstral representation of the resulting features [20]. One of the powerful properties of cepstrum is the fact that any periodicities, or repeated patterns, in a spectrum will be mapped to one or two specific components in the cepstrum. If a spectrum contains several harmonic series, they will be separated in a way similar to the way the spectrum separates repetitive time patterns in the waveform. The description of the different steps to exhibit features characteristics of an audio sample with MFCC is showed in Figure 6.

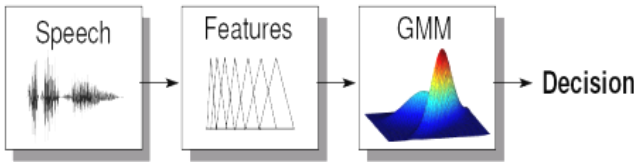

Fig. 5. Acoustic Speech Analysis.

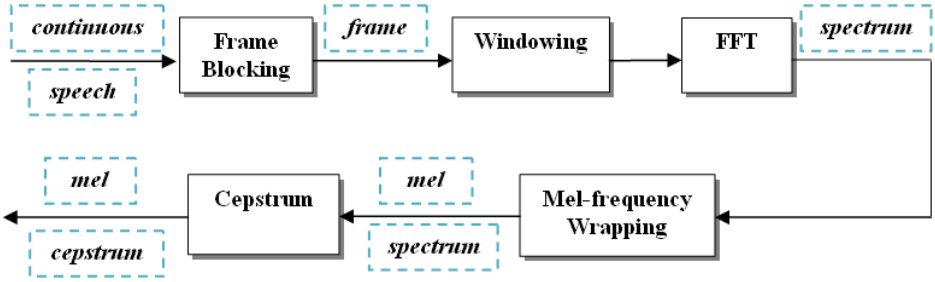

Fig. 6. MFCC calculation Block diagram [19].

The distribution of feature vectors for each person is modeled by a GMM. The parameters of the Gaussian mixture probability density function are estimated with Expectation Maximization (EM) algorithm [16]. Given a claim for person $C's$ identity and a set of feature vectors $X = \{\vec{x}_i\}_{(i=1)}^{N_v}$ supporting the claim, the average log likelihood of the claimant being the true claimant is calculated using :

$$\mathcal{L}\left(X|\lambda_C\right) = \frac{1}{N_V}\sum_{i=1}^{N_V} \log p\left(\vec{x}_i|\lambda_C\right) \tag{9}$$

where

$$p\left(\vec{x}|\lambda\right) = \sum_{j=1}^{N_M} m_j \mathcal{N}\left(\vec{x}; \overrightarrow{\mu_j}; \sum{}_j\right) \tag{10}$$

and

$$\lambda = \left\{ m_j, \overrightarrow{\mu_j}, \sum j \right\}_{j=1}^{N_M} \tag{11}$$

Here λ_C is the model for person C. N_M is the number of mixtures, m_j is the weight for mixture j (with constraint $\sum_{j=1}^{N_M} m_j = 1$), and $\mathcal{N}\left(\vec{x}; \overrightarrow{\mu_j}; \sum\right)$ is a multi-variate Gaussian function with mean $\overrightarrow{\mu}$ and diagonal covariance matrix $\sum$. Given a set $\{\lambda_b\}_{b=1}^{B}$ of B background person models for person C, the average log likelihood of the claimant being an impostor is found using :

$$\mathcal{L}\left(X|\lambda_{\bar{C}}\right) = \log\left[\frac{1}{B}\sum_{b=1}^{B}\exp\mathcal{L}\left(X|\lambda_b\right)\right] \tag{12}$$

The set of background person models is found using the method described in [9]. An opinion on the claim is found using :

$$o = \mathcal{L}\left(X|\lambda_C\right) - \mathcal{L}\left(X|\lambda_{\bar{C}}\right) \tag{13}$$

The opinion reflects the likelihood that a given claimant is the true claimant (i.e., a low opinion suggests that the claimant is an impostor, while a high opinion suggests that the claimant is the true claimant).

2.3. Signature Verification Systems

Handwritten signature is one of the first accepted civilian and forensic biometric identification technique in our society [21][22][23]. Human verification is normally very accurate in identifying genuine signatures. A signature verification system must be able to detect forgeries and at the same time reduce rejection of genuine signatures. The signature verification problem can be classified into categories : offline and online. Offline signature verification does not use dynamic information that is used extensively in online signature verification systems. This paper investigates the problem of offline signature verification. The problem of offline signature verification has been faced by taking into account three different types of forgeries : random forgeries, produced without knowing either the name of the signer or the shape of his signature ; simple forgeries, produced knowing the name of the signer but without having an example of his signature ; and skilled forgeries, produced by people who, looking at an original instance of the signature, attempt to imitate it as closely as possible.

Fig. 7. Wacom Graphire3 digitizing TabletPC.

Feature Extraction : The coordinate trajectories (x_n, y_n) and pressure signal p_n are the components of the unprocessed feature vectors $u_n = [x_n, y_n, p_n]^T$ extracted from the signature signal [24][29], where $n = 1, \cdots, N_s$ and N_s is the duration of the signature in time samples. Signature trajectories are then pre-processed by subtracting the centre of mass followed by rotation alignment based on the average path tangent angle. An extended set of discrete-time functions are derived from the pre-processed trajectories consisting of sample estimations of various dynamic properties. As s result, the parameterised signature O consists in the sequence of feature vectors $o_n = [x_n, y_n, p_n, \theta_n, v_n, \dot{x}_n, \dot{y}_n]^T$, $n = 1, \cdots, N_s$, where the upper dot notation represents an approximation to the first order time derivative and θ and v stand respectively for path tangent angle, path velocity magnitude.

$$v_i = \sqrt{\dot{x}_i^2 + \dot{y}_i^2} \text{ and } \theta = \arctan(\dot{y}_i, \dot{x}_i) \tag{14}$$

$$\dot{x}_i = x_i - x_{i-1} \text{ and } \dot{y}_i = y_i - y_{i-1} \tag{15}$$

A whitening linear transformation is finally applied to each discrete-time function so as to obtain zero mean and unit standard deviation function values. Seven dimensional feature vectors are used for GMM processing described in the following section. Figure 9 shows $x-$, $y-$, $p-$ and velocity signals of an example signature.

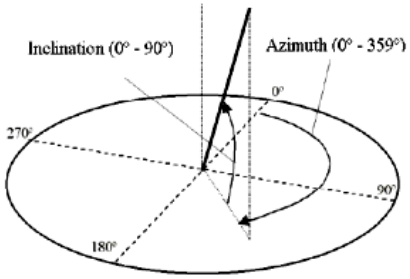

Fig. 8. Azimuth and inclination angles of the pen respect to the plane of the graphic card GD-0405U from Wacom Graphire3 digitizing TabletPC.

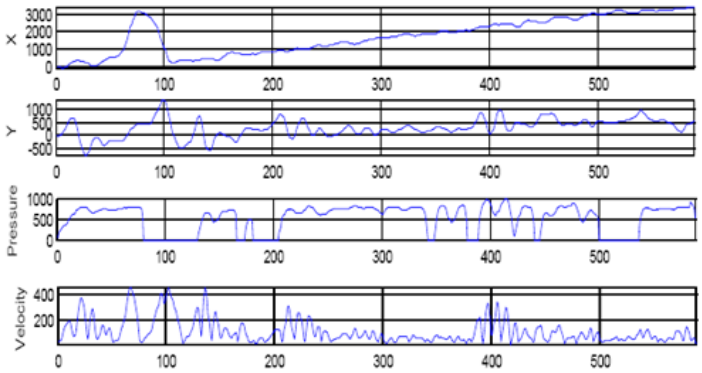

Fig. 9. Signals ($x-$, $y-$ position, pen pressure and velocity) of one signature fragment.

3. Multimodal Biometric Fusion Decision

The process of biometric user authentication can be outlined by the following steps [24] : a) acquisition of raw data, b) extraction of features from these raw data, c) computing a score for the similarity or dissimilarity between these features and a previously given set of reference features and d) classification with respect to the score, using a threshold. The results of the decision processing steps are *true or false (or accept/reject)* for verification purposes or the user identity for identification scenarios.

The fusion of different signals can be performed 1) at the raw data or the feature level, 2) at the score level or 3) at the decision level. These different approaches have advantages and disadvantages. *For raw data or feature level* fusion, the basis data have to be compatible for all modalities and a common matching algorithm (processing step c) must be used. If these conditions are met, the separate feature vectors of the modalities easily could be concatenated into a single new vector. This level of fusion has the advantage that only one algorithm for further processing steps is necessary instead of one for each modality. Another advantage of fusing at this early stage of processing is that no information is lost by previous processing steps. The main disadvantage is the demand of compatibility of the different raw data of features. The fusion at score level is performed by computing a similarity or dissimilarity (distance) score for each single modality. For joining of these different scores, normalization should be done. The straightforward and most rigid approach for fusion is the decision level. Here, each biometric modality results in its own decision ; in case of a verification scenario this is a set of *trues and falses*. From this set a kind of voting (majority decision) or a logical AND or OR decision can be computed. This level of fusion is the least powerful, due to the absence of much information. On the other hand, the advantage of this fusion strategy is the easiness and the guaranteed availability of all single modality decision results. In practice, score level fusion is the best-researched approach, which appears to result in better improvements of recognition accuracy as compared to the other strategies.

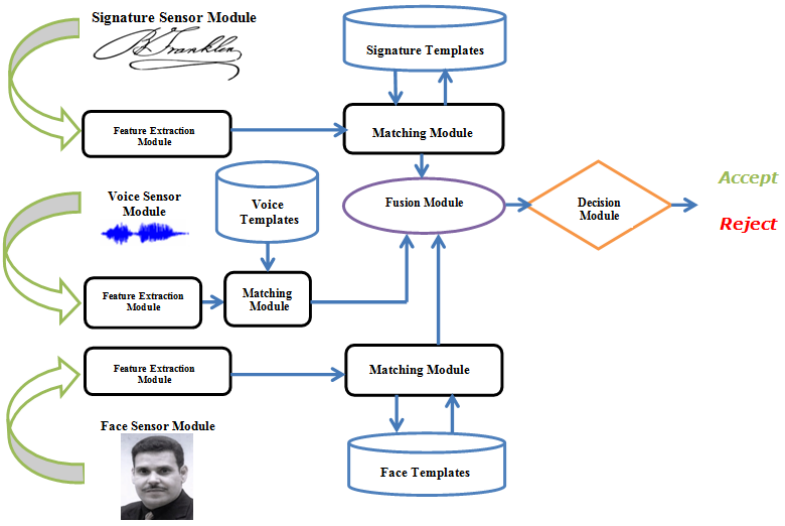

Fig. 10. Score Fusion Based Multimodal Biometric Verification System.

3.1. Adaptive Bayesian Method Based Score Fusion

Let $X = [X_1, X_2, \cdots, X_K]$ denote the match scores of K different biometric matchers, where X_K is the random variable representing the match score of the k^{th} matcher, $k = 1, 2, \cdots, K$. Let $f_{gen}(x)$ and $f_{imp}(x)$ be the conditional joint densities of the K match scores given the genuine and impostor classes, respectively, where $x = [x_1, x_2, \cdots, x_K]$. Suppose we need to assign the observed match score vector X to genuine or impostor class. Let Ψ be a statistical test for testing $H_0 : X$ corresponds to an impostor against $H_1 : X$ corresponds to a genuine user. Let $\Psi(x) = i$ imply that we decide in favor of H_i, $i = 0, 1$. The probability of rejecting H_0 when H_0 is true is known as the false accept rate (size or level of the test). The probability of correctly rejecting H_0 when H_1 is true is known as the genuine accept rate. The Neyman-Pearson theorem [25][26] states that :

1. For testing H_0 against H_1, there exists a test Ψ and a constant η such that :

$$P\left(\Psi(X) = 1 | H_0\right) = \infty \tag{16}$$

and

$$\Psi\left(x\right) = \begin{cases} 1, \text{ when } \frac{f_{gen}(x)}{f_{imp}(x)} \geq \eta \\ 0, \text{ when } \frac{f_{gen}(x)}{f_{imp}(x)} \geq \eta \end{cases} \tag{17}$$

2. If a test satisfies equations (14) and (15) for some η, then it is the most powerful test for testing H_0 against H_1 at level ∞.

According to the Neyman-Pearson theorem, given the false accept rate (FAR) ∞ , the optimal test for deciding whether a score vector X corresponds to a genuine user or an impostor is the likelihood ratio test given by equation (17). For a fixed FAR, it can select a threshold η such that the likelihood ratio test maximizes the genuine accept rate (GAR). Based on the Neyman-Pearson theorem, we are guaranteed that there does not exist any other decision rule with a higher GAR. However, this optimality of the likelihood ratio test is guaranteed only when the underlying densities are known. In practice, it estimate the densities $f_{gen}(x)$ and $f_{imp}(x)$ from the training set of genuine and impostor match scores, respectively and the performance of likelihood ratio test will depend on the accuracy of these estimates [24][27].

3.1.1. Estimation of Match Score Densities

Gaussian mixture model (GMM) has been successfully used to estimate arbitrary densities and it is used for estimating the genuine and impostor score densities [16][24].

Let $\Phi^K\left(x; \mu, \sum\right)$ be the K-variate Gaussian density with mean vector μ and covariance matrix $\sum$, i.e., $\Phi^K\left(x; \mu, \sum\right) = (2\pi)^{-K/2} |\sum|^{-1/2} exp\left(-\frac{1}{2}(x-\mu)^T \sum^{-1}(x-\mu)\right)$.The estimates of $f_{gen}(x)$ and $f_{imp}(x)$ are obtained as a mixture of Gaussians as follows.

$$\hat{f}_{gen}\left(x\right) = \sum_{j=1}^{M_{gen}} P_{gen,j} \Phi^K\left(x; \mu_{gen,j}, \sum{}_{gen,j}\right) \tag{18}$$

$$\hat{f}_{imp}(x) = \sum_{j=1}^{M_{imp}} P_{imp,j} \Phi^K \left(x; \mu_{imp,j}, \sum imp,j \right) \tag{19}$$

Where M_{gen} (M_{imp}) is the number of mixture components used to model the density of the genuine (impostor) scores,$P_{gen,j}$ ($P_{gen,j}$) is the weight assigned to the j^{th} mixture component in $\hat{f}_{imp}(x)$ ($\hat{f}_{imp}(x)$), $\sum_{j=1}^{M_{gen}} P_{gen,j} = \sum_{j=1}^{M_{imp}} P_{imp,j} = 1$. Selecting the appropriate number of components is one of the most challenging issues in mixture density estimation ; while a mixture with too many components may result in over-fitting, a mixture with too few components may not approximate the true density well. The GMM fitting algorithm automatically estimates the number of components and the component parameters using EM algorithm and the minimum message length criterion [16][29].

Maximum Likelihood Parameter Estimation : Given a set of observation data in a matrix X and a set of observation parameters θ the ML parameter estimation aims at maximizing the likelihood $L(\theta)$ or log likelihood of the observation data $X = [X_1, X_2, \cdots, X_K]$.

$$\hat{\theta} = \arg\max_{\theta} L(\theta). \tag{20}$$

Assuming that it has independent, identically distributed data, it can write the above equations as :

$$L(\theta) = p(X|\theta) = p(X_1, \ldots, X_n|\theta) = \prod_{i=1}^{n} p(X_i|\theta) \tag{21}$$

The maximum for this function can be find by taking the derivative and set it equal to zero, assuming an analytical function.

$$\frac{\partial}{\partial\theta} L(\theta) = 0 \tag{22}$$

The incomplete-data log-likelihood of the data for the mixture model is given by :

$$L(\theta) = log(X|\theta) = \sum_{i=1}^{N} log(x_i|\theta) \tag{23}$$

which is difficult to optimize because it contains the log of the sum. If it considers X as incomplete, however, and posits the existence of unobserved data items $Y = \{y_i\}_{i=1}^{N}$ whose values inform us which component density generated each data item, the likelihood expression is significantly simplified. That is, it assume that $y_i \in \{1 \cdots K\}$ for each i,

and $y_i = k$ if the i^{th} sample was generated by the k^{th} mixture component. If it knows the values of Y, it obtains the complete-data log-likelihood, given by :

$$\begin{aligned} L(\theta, Y) &= \log p(X, Y|\theta) && (24)\\ &= \sum_{i=1}^{N} \log p(x_i, y_i|\theta) && (25)\\ &= \sum_{i=1}^{N} \log \left(p(y_i|\theta)\, p(x_i|y_i, \theta)\right) && (26)\\ &= \sum_{i=1}^{N} \left(\log p_{yi} + \log g\left(x_i|\mu_{yi}, \sum_{yi}\right)\right) && (27) \end{aligned}$$

Which, given a particular form of the component densities, can be optimized using a variety of techniques [8].

EM Algorithm : The expectation-maximization (EM) algorithm [22][29][24][31] is a procedure for maximum-likelihood (ML) estimation in the cases where a closed form expression for the optimal parameters is hard to obtain. This iterative algorithm guarantees the monotonic increase in the likelihood L when the algorithm is run on the same training database.

The probability density of the Gaussian mixture of k components in R^d can be described as follows :

$$\Phi(x) = \sum_{i=1}^{N} \pi_i \emptyset(x|\theta_i)\, \forall x \in R^d \quad (28)$$

Where $\phi(x|\theta_i)$ is a Gaussian probability density with the parameters $\theta_i = (m_i, \sum_i)$, m_i is the mean vector and $\sum_i$ is the covariance matrix which is assumed positive definite given by :

$$\emptyset(x|\theta_i) = \emptyset\left(x|m_i, \sum_i\right) = \frac{1}{(2\pi)^{\frac{n}{2}} |\sum_i|^{\frac{1}{2}}} e^{-\frac{1}{2}(x-m_i)^T \sum_i^{-1}(x-m_i)} \quad (29)$$

and $\pi_i \in [0, 1](i = 1, 2, \cdots, k)$ are the mixing proportions under the constraint $\sum_{i=1}^{k} \pi_i = 1$. If it encapsulate all the parameters into one vector : $\Theta_k = (\pi_1, \pi_2, \ldots, \pi_k, \theta_1, \theta_2, \cdots, \theta_k)$, then , according to Eq. (27), the density of Gaussian mixture can be rewritten as :

$$\Phi(x|\Phi_i) = \sum_{i=1}^{k} \pi_i \emptyset(x|\theta_i) = \sum_{i=1}^{k} \pi_i \emptyset\left(x|m_i, \sum_i\right) \quad (30)$$

For the Gaussian mixture modeling, there are many learning algorithms. But the EM algorithm may be the most well-known one. By alternatively implementing the E-step

to estimate the probability distribution of the unobservable random variable and the M-step to increase the log-likelihood function, the EM algorithm can finally lead to a local maximum of the log-likelihood function of the model. For the Gaussian mixture model, given a sample data set $S = \{x_1, x_2, \cdots, x_N\}$ as a special incomplete data set, the log-likelihood function can be expressed as follows :

$$\log p\left(S|\Theta_k\right) = \log \prod_{t=1}^{N} \emptyset\left(x_t|\Theta_k\right) = \sum_{t=1}^{N} \log \sum_{i=1}^{k} \pi_i \emptyset\left(x_t|\theta_i\right) \tag{31}$$

which can be optimized iteratively via the EM algorithm as follows :

$$P\left(j|x_t\right) = \frac{\pi_j \emptyset\left(x_t|\theta_j\right)}{\sum_{i=1}^{k} \pi_i \emptyset\left(x_t|\theta_i\right)} \tag{32}$$

$$\pi_j^+ = \frac{1}{N} \sum_{t=1}^{N} P\left(j|x_t\right) \tag{33}$$

$$\mu_j^+ = \frac{1}{\sum_{t=1}^{N} P\left(j|x_t\right)} \sum_{t=1}^{N} P\left(j|x_t\right) x_t, \tag{34}$$

$$\sum\nolimits_j^+ = \frac{1}{\sum_{t=1}^{N} P\left(j|x_t\right)} \sum_{t=1}^{N} P\left(j|x_t\right) \left(x_t - \mu_j^+\right) \left(x_t - \mu_j^+\right)^T \tag{35}$$

Although the EM algorithm can have some good convergence properties in certain situations, it certainly has no ability to determine the proper number of the components for a sample data set because it is based on the maximization of the likelihood.

4. Experiments and Results

The experiments were performed using still faces, signatures and audio database extracted from video, which is encoded in raw UYVY. AVI 640 x 480, 15.00 fps with uncompressed 16bit PCM audio ; mono, 32000 Hz little endian. Uncompressed PNG files are extracted from the video files for feeding the face detection algorithms. The capturing devices for recording the video and audio data were : Allied Vision Technologies AVT marlin MF-046C 10 bit ADC, 1/2" (8mm) Progressive scan SONY IT CCD ; and Shure SM58 microphone. Frequency response 50 Hz to 15000 Hz. Unidirectional (Cardiod) dynamic vocal microphones. Thirty subjects were used for the experiments in which twenty-six are males and four are females. For each subject, 30 signatures (with dat header) are used. Each line of a (.dat files) consists of four comma separated integer values for the sampled x- and y-position of the pen tip, the pen pressure and the timestamp (in ms) ; the lines with values of -1 for x, y and pressure represent a pen-up/pen-down event ; The device

used for recording the handwriting data was a Wacom Graphire3 digitizing tablet. Size of sensing surface is 127.6mm x 92.8mm. With spatial resolution of 2032 lpi (lines per inch), able to measure 512 degrees of pressure. The signature data is acquired with a non-fixed sampling rate of about 100Hz. The audio is extracted as 16 bit PCM WAV file (with wav header), sampled at 16000 Hz, mono little endian. For the audio six multi-lingual (.wav files) of one minute each recording were used for each subject. The database obtained from eNTERFACE 2005 [32]. Thirty subjects were used for the experiments in which twenty-five are males and five are females. For face experts, ninety-six face images from a subject were randomly selected to be trained and projected into Eigen space, and the other twenty-four samples were used for the subsequent validation and testing. Similarly, four samples were used in speech experts for the modeling (training) ; two samples were used for the subsequent validation and testing. For signature experts, twenty four signatures from a subject were randomly selected for training, and the other six samples were used for the subsequent validation and testing. Three sessions of the face database, signature and speech database were used separately. Session one was used for training the speech and face experts. Each expert used ten mixture client models. To find the performance, Sessions two and three were used for obtaining expert opinions of known impostor and true claims.

Performance Criteria : The basic error measure of a verification system is false rejection rate (FRR) and false acceptance rate (FAR) as defined in the following equations :

False Rejection Rate ($\mathbf{FRR}_i$) : is an average of number of falsely rejected transactions. If n is a transaction and $x(n)$ is the verification result where 1 is falsely rejected and 0 is accepted and N is the total number of transactions then the personal False Rejection Rate for user i is

$$FRR_i = \frac{1}{N}\sum_{n=1}^{N} x(n) \tag{36}$$

False Acceptance rate ($\mathbf{FAR_i}$) is an average of number of falsely accepted transactions. If n is a transaction and x(n) is the verification result where 1 is a falsely accepted transaction and 0 is genuinely accepted transaction and N is the total number of transactions then the personal False Acceptance Rate for user i is

$$FAR_i = \frac{1}{N}\sum_{n=1}^{N} x(n) \tag{37}$$

Both FRRi and FARi are usually calculated as averages over an entire population in a test. If P is the size of populations then these averages are

$$FRR = \frac{1}{P}\sum_{i}^{P} FRR_i \tag{38}$$

$$FAR = \frac{1}{P}\sum_{i}^{P} FAR_i \tag{39}$$

Equal Error Rate (EER), is an intersection where FAR and FRR are equal at an optimal threshold value. This threshold value shows where the system performs at its best.

As a common starting point, classifier parameters were selected to obtain performance as close as possible to EER on clean test data (following the standard practice in the face and speaker verification area of using EER as a measure of expected performance). A good decision is to choose the decision threshold such as the false accept equal to the false reject rate. In this paper it uses the Detection Error Tradeoff (DET) curve to visualize and compare the performance of the system (see Figure 11).

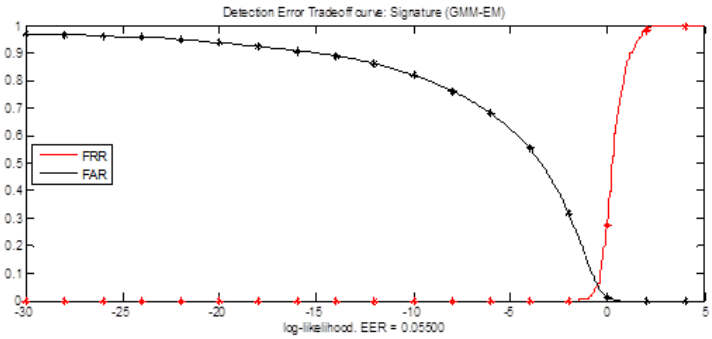

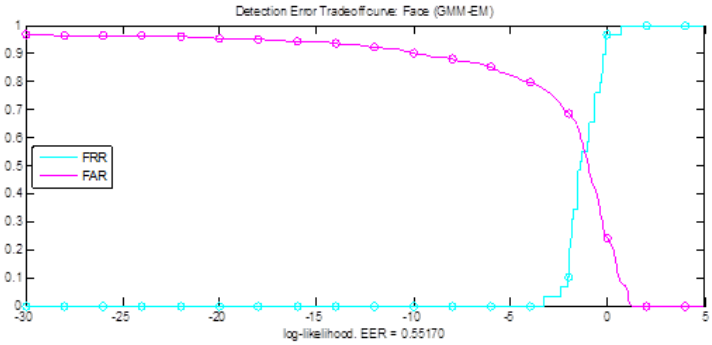

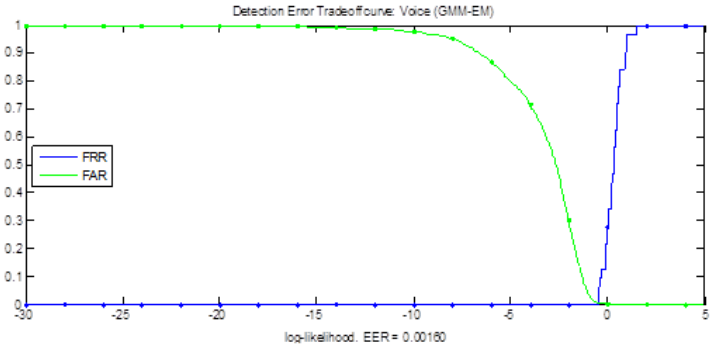

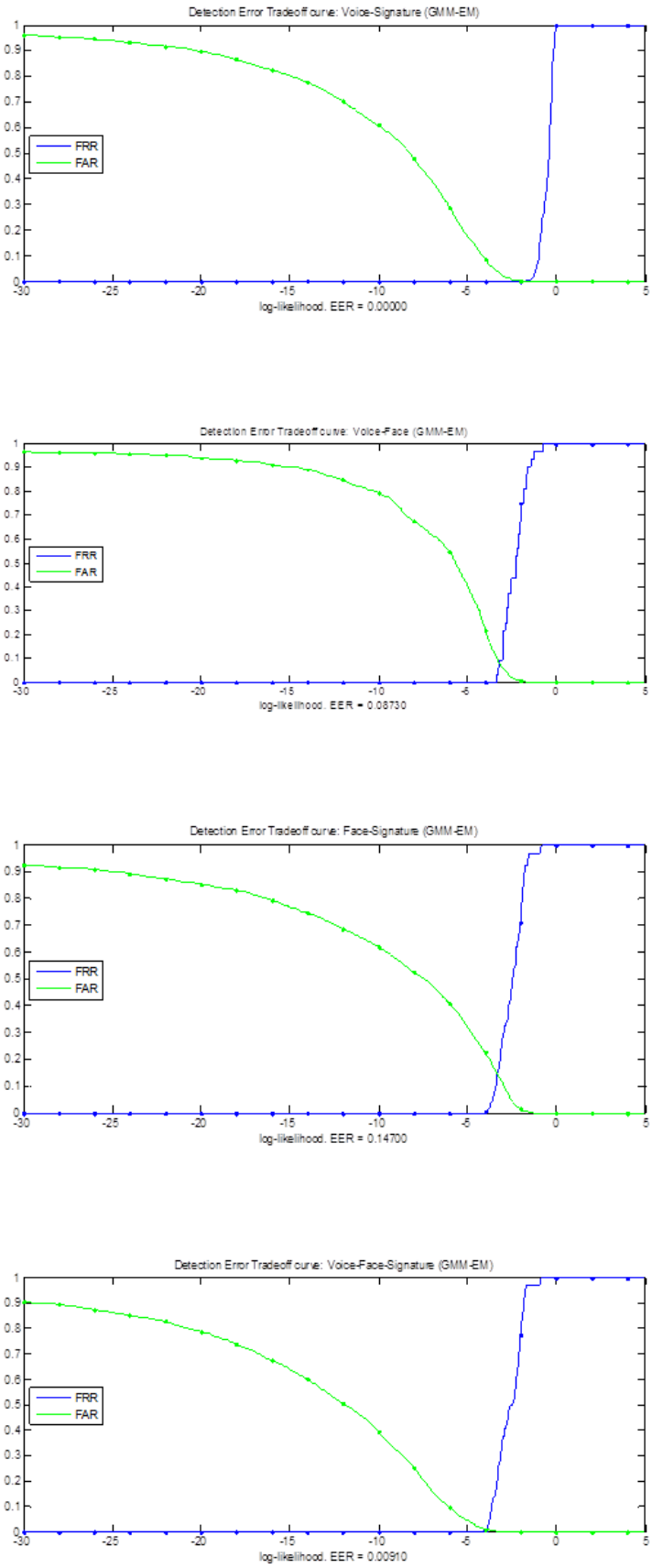

Fig. 11. Detection error tradeoff curves.

5. Discussion and Conclusions

The question that always arises is how it can obtain the "best" (in terms of accuracy) ; the solution is fusion. It is well known that the "best" fusion solution is one that satisfies the Neyman-Pearson (NP) criterion [33]. The NP criterion characterizes the fusion solution that maximizes the True Accept Rate (TAR) for a fixed value of False Accept Rate (FAR) [25][28][33].

In the case of a verification system, two error rates are evaluated which vary in opposite directions : the false rejection rate FRR (rejection of a legitimate user called "the client") and the false acceptance rate FAR (acceptance of an impostor) [33]. The decision of acceptance or rejection of a person is thus taken by comparing the answer of the system to a threshold (called the decision threshold). The values of FAR and FRR are thus dependent on this threshold which can be chosen so as to reduce the global error of the system [30][33]. The decision threshold must be adjusted according to the desired characteristics for the application considered. High security applications require a low FAR which has the effect of increasing the FRR, while Low security applications are less demanding in terms of FAR, EER denotes Equal Error Rate and it's the point where (FAR=FRR). This threshold must be calculated afresh for each application, to adapt it to the specific population concerned [30][33]. This is done in general using a small database recorded for this purpose.

Performance capabilities have been traditionally shown in the form of ROC (receiver- or relative-operating characteristic) plots [33], in which the probability of a false-acceptance is plotted versus the probability of a false-rejection for varying decision thresholds. Unfortunately, with ROC plots, curves corresponding to well-performing systems tend to bunch together near the lower left corner, impeding a clear visualization of competitive systems [33].

More recently, a variant of an ROC plot, the detection error tradeoff (DET) plot has been used, which plots the same tradeoff using a normal deviate scale. This has the effect of moving the curves away from the lower left corner when performance is high and producing linear curves, making system comparisons easier [33]. Although the complete DET curve is needed to fully describe system error tradeoffs, it is desirable to report performance using a single number. Often the equal-error-rate (EER), the point on the DET curve where the FA rate and FR rate are equal, is used as this single summary number [33]. However, the suitability of any system or techniques for an application must be determined by taking into account the various costs and impacts of the errors and other factors such as implementations and lifetime support costs and end-user acceptance issues [30][33].

This paper has presented a human authentication method combined dynamic face, online signature and text independent speech information in order to improve the problem of single biometric authentication, since single biometric authentication has the fundamental problems of high False Accept Rate (FAR) and False Reject Rate (FRR). It has presented a framework for fusion of match scores in multi-modal biometric system based on adaptive Bayesian method. The product of likelihood ratio based fusion rule with (GMM-EM) based density estimation achieves a significant recognition rates. As a result presented a combined authentication method can provide a stable authentication rate and it overcomes

the limitation of a single mode system. Based on the experimental results, it has shown that EER can be reduced down significantly between the dynamic face, on-line signature mode and a combined face-voice-signature mode.

REFERENCES

[1] S. Gleni & P. Petratos, "DNA Smart Card for Financial Transactions", The ACM Student Magazine 2004, http ://www.acm.org.

[2] G. Chetty and M. Wagner, "Audio-Visual Multimodal Fusion for Biometric Person Authentication and Liveness Verification", Copyright © 2006, Australian Computer Society, Inc. This paper appeared at the NICTA-HCSNet Multimodal UserInteraction Workshop (MMUI2005), Sydney, Australia.

[3] N. Poh and S. Bengio, "Database, Protocol and Tools for Evaluating Score-Level Fusion Algorithms in Biometric Authentication", IDIAP RR 04-44, August 2004, a IDIAP, CP 592, 1920 Martigny, Switzerland.

[4] S. Ben-Yacoub, Y. Abdeljaoued, and E. Mayoraz, "Fusion of Face and Speech Data for Person Identity Verification", IEEE TRANSACTIONS ON NEURAL NETWORKS, VOL. 10, NO. 5, SEPTEMBER 1999.

[5] H. J. Korves, L. D. Nadel, B. T. Ulery and D. M. Bevilacqua Masi, "Multi-biometric Fusion : From Research to Operations", MTS MitreTek Systems, sigma summar 2005, pp. 39-48, http ://www.mitretek.org/home.nsf/Publications/SigmaSummer2005.

[6] K. Nandakumar, Y. Chen, S. C. Dass and A. K. Jain, "Biometric Score Fusion : Likelihood Ratio, Matcher Correlation and Image Quality", March 2007 DRAFT.

[7] A. Jain, K. Nandakumar and A. Ross, "Score normalization in multimodal biometric systems", THE JOURNAL OF PATTERN RECOGNITION SOCIETY, ELSEVIER 2005.

[8] Kittler J., Hatef M., Duin R. P. W. and Matas J., "On combining classifiers", IEEE Transactions on Pattern Analysis and Machine Intelligence, 20(3) : 226–239. 1998.

[9] R. Snelick, U. Uludag, A. Mink, M. Indova and A. Jain, "Large Scale Evaluation of Multimodal Biometric Authentication Using State-of-the-Art Systems", IEEE Transactions on Pattern Analysis and Machine Intelligence, Vol. 27, No. 3, Mar 2005, pp 450-455.

[10] A. Teoh, S. A. Samad and A. Hussain, "Nearest Neighbourhood Classifiers in Biometric Fusion", International Journal of The Computer, the internet and management Vol. 12 No. 1, 2004, pp 23-36.

[11] Y. Elmir, Z. Elberrichi and R. Adjoudj, "Multimodal Biometric Using a Hierarchical Fusion of a Person's Face, Voice and Online Signature", Journal of Information Processing Systems (JIPS), 2014.

[12] M. Kaur, A. Girdhar and M. Kaur, "Multimodal Biometric System Using Speech and Signature Modalities", International Journal of Computer Applications (IJCA) Vol. 5, No.12, August 2010.

[13] Corradini1, M. Mehta1, N.O. Bernsen1, J. C. Martin2,3, S. Abrilian2, "MULTIMODAL INPUT FUSION IN HUMAN-COMPUTER INTERACTION", On the Example of the NICE Project 2003. 1Natural Interactive Systems Laboratory (NISLab), University of Southern Denmark, DK-Odense M, Denmark, 2Laboratory of Compu-

ter Science for Mechanical and Engineering Sciences, LIMSI-CNRS, F-91403 Orsay, France, 3Montreuil Computer Science Institute (LINC-IUT), University Paris 8, F-93100 Montreuil, France.

[14] Y. Zana, Roberto M. Cesar-Jr, Rogerio S. Feris, and M. Turk, "Face Verification in Polar Frequency Domain : A Biologically Motivated Approach", ISVC 2005, LNCS 3804, pp. 183–190, 2005, C Springer-Verlag Berlin Heidelberg 2005.

[15] M. Turk and A. Pentland, "Eigen faces for Recognition", Journal of Cognitive Neuroscience, Vol.3, No.1, pp. 71-86, 1991.

[16] P. Paalanen, "Bayesian classification using gaussian mixcute model and EM estimation : implementation and comparisons", Information Technology Project, 2004, Lappeenranta, June 23, 2004, http ://www.it.lut.fi/project/gmmbayes/.

[17] C. Sanderson, S. Bengio, H. Bourlard, J. Mariéthoz, R. Collobert, Mohamed F. BenZeghiba, F. Cardinaux, and S. Marcel, "SPEECH & FACE BASED BIOMETRIC AUTHENTICATION AT IDIAP", Dalle Molle Institute for Perceptual Artificial Intelligence (IDIAP). 2003.

[18] C. Vielhauer, S. Schimke, V. Thanassis and Y. Stylianou , "Fusion Strategies for Speech and Handwriting Modalities in HCI", Multimedia on Mobile Devices, Proc. of SPIE-IS & T Electronic Imaging, Vol. 5684 © 2005.

[19] L. L. Mølgaard and K. W. Jørgensen, "Speaker Recognition : Special Course", IMM_DTU December 14, 2005.

[20] S. Davis and P. Mermelstein, "Comparison of parametric representations for monosyllabic word recognition in continuously spoken sentences", IEEE Transactions on Acoustics, Speech and Signal Processing, (4) :357–366, 1980.

[21] M. SOLTANE, N. DOGHMANE, N. GUERSI, "State of the Art : Signature Biometrics Verification", BRAIN. Broad Research in Artificial Intelligence and Neuroscience. Vol 1, N 2, Romania 2010. http ://www.edusoft.ro/brain.

[22] M. SOLTANE, B. MIMEN, "Soft Decision Level Fusion Approach to a Combined Behavioral Speech Signature Biometrics Verification", International Journal of Signal Processing, Image Processing and Pattern Recognition – IJSIP, Vol.5, No. 5 South Korea (March 2013). http ://www.sersc.org/journals/IJSIP/vol5_no5.php.

[23] J. Richiardi, J. Fierrez-Aguilar, J. Ortiga-Garcia and A. Drygajlo, "On-line signature verification resilience to packet loss in IP networks", second COST 275 WORKSHOP Biometrics on the Internet : Fundamentals, Advances and Applications. University of Vigo, Vigo-Spain 25-26 March 2004.

[24] K. Veeramachaneni, L. Ann Osadciw and P. K. Varshney, "An Adaptive Multimodal Biometric Management Algorithm", IEEE TRANSACTIONS ON SYSTEMS, MAN, AND CYBERNETICS-PART C : APPLICATIONS AND REVIEWS, VOL. 35, NO. 3, AUGUST 2005.

[25] Van Trees, Harry L., "Detection, Estimation, and Modulation Theory", Part I, John Wiley and Sons, 1968.

[26] Qing Yan and Rick S. Blum, "Distributed Signal Detection under the Neyman-Pearson Criterion", EECS Department Lehigh University Bethlehem, PA 18015.

[27] K. Nandakumar, Yi Chen, Sarat C. Dass and Anil K. Jain, "Likelihood Ratio Based Biometric Score Fusion", IEEE Transactions on Pattern Analysis and Machine Intelligence, 2007.

[28] H. J. Korves, L. D. Nadel, B. T. Ulery, D. M. Bevilacqua Masi, “Multi-biometric Fusion : From Research to Operations”, MTS MitreTek Systems, sigma summar 2005, pp. 39-48, http ://www.mitretek.org/home.nsf/Publications/SigmaSummer2005.

[29] P. Paalanen, J.-K. Kamarainen, J. Ilonen and H. Kälviäinen, "Feature Representation and Discrimination Based on Gaussian Mixture Model Probability Densities : Practices and Algorithms", Department of Information Technology, Lappeenranta University of Technology, FI-53851 Lappeenranta, Finland 2005.

[30] Van Trees and Harry L., "Detection, Estimation, and Modulation Theory", Part I, John Wiley and Sons, 1968.

[31] B. Dorizzi Biometrics at the frontiers, assessing the impact on Society Technical impact of Biometrics, Background paper for the Institute of Prospective Technological Studies, DG JRC – Sevilla, European Commission, January 2005.

[32] Y. Stylianou, Y. Pantazis, F. Calderero, P. Larroy, F. Severin, S. Schimke, R. Bonal, F. Matta, and A. Valsamakis, "GMM-Based Multimodal Biometric Verification", eNTERFACE 2005 The summer Workshop on Multimodal Interfaces July 18th – August 12th, Facultè Polytechnique de Mons, Belgium.

[33] M. SOLTANE and B. MIMEN, "MULTI-MODAL BIOMETRIC AUTHENTICATIONS : CONCEPT ISSUES AND APPLICATIONS STRATEGIES", International Journal of Advanced Science and Technology – IJAST, Vol.49, South Korea (December 2012). http ://www.sersc.org/journals/IJAST/vol48.php.

Author

Mohamed SOLTANE (Assoc. Prof. Dr.) received the M.Eng. degree in Electronics from Badji-Mokhtar University of Annaba-Algeria, in 1995 and the M.Sc. degree in Electrical and Electronics Engineering from UKM Malaysia in 2005, and the Ph.D. degrees in Electronics from Badji-Mokhtar University of Annaba-Algeria, in 2010. He is currently an Associate Professor at Electrical Engineering & Computing Department, Faculty of Sciences & Technology, DOCTOR YAHIA FARES UNIVERSITY OF MEDEA, ALGERIA. His research interests include statistical pattern recognition, biometric authentication, cryptography and quantum computing, computer vision and machine learning and microcomputer based system design...

ISSN : 2335 - 1357

Mediterranean Journal of Modeling and Simulation

Med. J. Model. Simul. 04 (2015) 037-050

Fatigue life prediction of package of suspension automotive under random vibration based on road roughness

Kazem Reza Kashyzadeh [a] *, Mohammad Jafar Ostad-Ahmad-Ghorabi [b] , Alireza Arghavan [b]

[a] Young Researchers and Elite Club, Semnan Branch, Islamic Azad University, Semnan, Iran.
[b] Mechanical Engineering Department, Islamic Azad University, Semnan-branch, Semnan, Iran.

ARTICLE INFO

Article history :
Received June 2015
Accepted July 2015

Keywords :
Fatigue ;
Random vibrations ;
Road roughness ;
Suspension system ;
Pitman arm ;
Hub wheel ;
Suspension system.

ABSTRACT

The impact of a suitable suspension system for passenger comfort and vehicle steering is an obvious order and direct impact on the safety of passengers must be considered, to do so different kinds of tests must be exerted, one of these is fatigue testing which is one of the most significant ones. Another issue is the high cost in practical ways, and to cope with this issue various ways must be assessed and analyzed, one of the best and the most efficient ways is modelling and testing in virtual software environments. In the present paper, predict fatigue life of suspension component and package of automotive suspension are the main purposes. First, using MATLAB software, road roughness according to the intercity roads for constant vehicle velocity (100Km/h) has been studied. After that frequency response of components has been analysed, its critical points determined to calculate the fatigue life of the part, and the amount of critical stress obtained based on Von Misses, Tresca and Max Principle criterion for a quarter car model (passive suspension System in 206 Peugeot). Fatigue life of the vehicle components are calculated in terms of kilo-Meters in specialized fatigue software such as 116944, 92638.9, 46388.9 and 191388.9 Km respectively wheel hub, pitman arm, suspension arm and package of suspension. Finally, to prove the given results of the finite element method compared with reported results by other researchers and the results match very well with those.

1. Introduction

Investigating Fatigue is one the most important factors in designing most mechanical structure. The reason is that, in many cases, the specimens of the structure break down without any warning or alarm. However, Fatigue is the main reason for the failure of most mechanical parts during operation [1]. Such as :

*Email : kazem.kashyzadeh@gmail.com

– Comet airliner crashed in the Mediterranean Sea.
– Catastrophic crash of jet F-111 that has an important role to development of B-1 bomber base on fracture mechanics [1].
– Plazant Bridge in West Virginia failed without any warning [2].

Vibration Responses have a great importance in all fields of science and engineering, so study of the material behavior under random vibrations is necessary in automotive industry.

Suspension systems are part of chassis that have an important role in the behavior and performance of vehicle. Any suspension system consists of 4 parts such as springs, shock absorbers, suspension mechanism and interface link connection that are responsible for the following key tasks [3] :

Create a separately conditions of chassis from road roughness to comfort and safe travel.

Create a permanent contact between tire and road conditions in order to provide Proper tire performance on vehicle longitudinal and lateral movement.

Create proper conditions for the stability of the vehicle with good behavior during the rolling and heading movement (degree of freedom decrease).

ElMadany in 1990 has been analyzed the efficiency of passive suspension system of transport vehicles like trucks that obtained the power spectral density function of road roughness on the vehicle axles (front and rear axles) by linear and nonlinear springs [4].

Bishop et al. has been studied the finite element analysis of fatigue failures that occurred in several of the industry specimens (railroads, pitman arm of suspension system of vehicle, etc.) [5]. Badih in 2002 was presented a complete design and construction of a wheel of the race car including geometric model of the suspension and its components (hub, pitman arm, etc) [6].

Haiba et al. are discussed in pitman arm's suspension to develop optimization algorithm based on fatigue life. In this research used 1/2 car model movement with constant velocity ($34Km/h$) on the paved asphalt road and under 3 different loads such as static, transient dynamic and harmonic with constant amplitude. So, predict fatigue life by using superposition of 3 directions of concentrated load [7]. After that Nadot study of the fatigue failure of pitman arm's suspension with multi axial loading that is discussed on the defects in the heat treatment and its effects on low and high cycle fatigue [8].

Svensson et al. predict fatigue life of suspension arm [9] and Buciumeanu developed the design of suspension components in corresponding wear and fatigue. Reports that there is more damage in the screw, so, published several solutions to decrease its effect [10].

Soleimani eyvari elicited transferred shocks to the vehicle on a paved road by experimental data [11]. Martinez measured and analyzed vibration behavior in terms of speed for truck transportation in Spain [12]. Colombo studied the unusual fracture of McPherson suspension and found that critical stress on the top of connection linking between pitman arm and suspension arm is about $358Mpa$ [13].

Borg reported An Approach to Using Finite Element Models to Predict Suspension Member Loads in a Formula SAE Vehicle in his Master thesis of Science in Mechanical Engineering at University of Technological Virginia [14].

Rahman et al. investigated to predict Fatigue Life of Lower Suspension Arm Using Strain-Life Approach [15]. Breytenbach optimized vehicle suspension characteristics for increased structural fatigue life [16] and Tung investigate Optimization of the exponential

stabilization problem in active suspension system using PSO Method [17].

Schwab published one chapter about how can predict fatigue life base on random vibration loading. So, used 3D modeling and assumes 3 function for each direction to obtain random vibration response versus stress history and RMS function [18].

In most published studies, investigate fatigue life of suspension component separately but in the present research, investigate package of suspension system in addition suspension components such as wheel hub, pitman arm, and triangular suspension arm. Another innovation of this research is applying random vibration response to predict fatigue life directly, however in the past apply uniaxial or biaxial load, so use superposition law to predict it. This advantage should be noted that in order to achieve safety data, we are considered vehicle velocity as an influence parameter on entering loads to it from roads.

2. Road Roughness Simulation

Among the factors that are important in simulating a suspension system and achieving the desired response are the inputs of that system which are the natural inputs of road roughness. Generally, to study the characteristics of passenger cars, the excitations of the ground are used in different forms of sine waves, step functions or triangular waves. Later, it was found out that road surface profile would be more practical and realistic as a random function which it is closer to reality. So, International Organization for Standardization (ISO) has proposed a road roughness classification (classes A-H) based on the power spectral density functions such as PSD that is presented parametrically in Table 1.

Table 1. Parametrical classification of road roughness suggested by international standard organization ISO [19-20].

Road Class	**Degree of Roughness Range**	$\mathbf{S}_g(\Omega_0), \mathbf{10^{-6}m^2/cycles/m}$ **Geometric Mean**
A (Very Good)	<8	4
B (Good)	8 – 32	16
C (Average)	32 – 128	64
D (Poor)	128 – 512	256
E (Very Poor)	512 – 2048	1024
F	2048 – 8192	2048
G	8192 – 32768	4096
H	More than 32768	16384

In the classification of the road surface roughness suggested by the international organization for standardization (ISO), relationships between the power spectral density function $Sg(\Omega)$ and spatial frequency Ω for different roads can be expressed with two straight lines and different slopes in the logarithmic scale that for two different ranges of frequencies are as follows [20-21] :

For $\Omega \leq \Omega_0 = \frac{1}{2\pi}$Cycles/m

$$Sg\left(\Omega\right) = Sg\left(\Omega_0\right) \times \left(\frac{\Omega}{\Omega_0}\right)^{-N_1} \tag{1}$$

And for $\Omega > \Omega_0 = \frac{1}{2\pi}$Cycles/m

$$Sg\left(\Omega\right) = Sg\left(\Omega_0\right) \times \left(\frac{\Omega}{\Omega_0}\right)^{-N_2} \tag{2}$$

Values of $Sg\left(\Omega_0\right)$ in the spatial frequency $\Omega_0 = 1/2\pi\ Cycle/m$ for different roads are presented in Table 1 and constants of N_1 and N_2 are respectively considered as 2.0 and 1.5.

In the present research, Firstly By using a quarter Car Model of passive suspension of 206 Peugeot in according road classification ISO 2631-1 is achieved road roughness as PSD function in constant speed of car ($V = 100Km/h$) by using MATLAB Code [22-23] and compared with Road Classification suggested by ISO as shown in Figure 1.

In the next step, vertical displacement of road in classification A until E in term of travel length as shown in Figure 2.

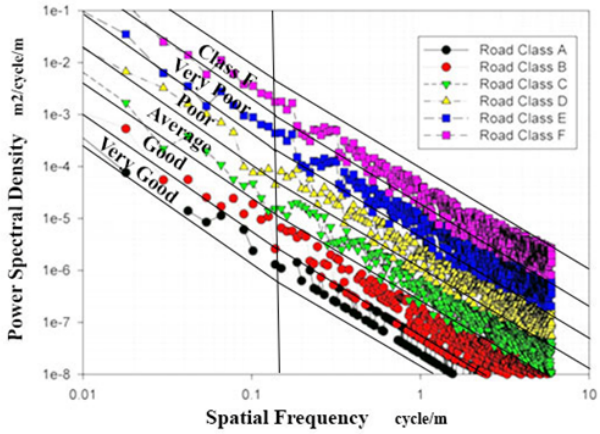

Fig. 1. Compared classification of surface roughness simulated in MATLAB Software and suggested by ISO [24-25].

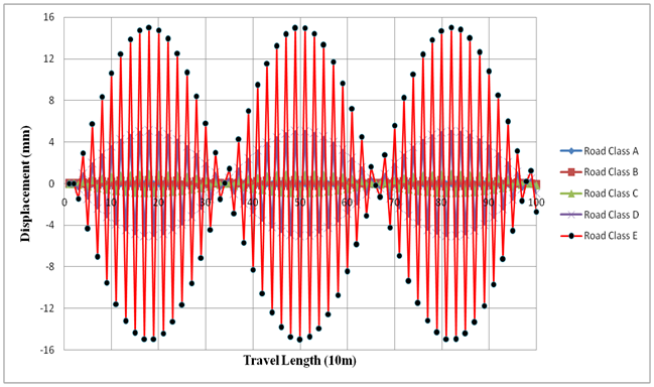

Fig. 2. Road Roughness function in terms of Travel Length in different Road Classification by ISO with Constant Velocity 100 Km/h [22].

For vehicle vibration Analysis, it is more convenient to express the power spectral density of surface profiles in terms of the temporal frequency in Hz rather than in terms of the spatial frequency, since vehicle vibration is a function of time. The transformation of the spatial frequency Ω in Cycles/m to the temporal frequency f in Hz is that of the speed of the vehicles [20-21] :

$$f\,[Hz] = \Omega\,[Cysle/m] \times V\,[m/s] \tag{3}$$

The transformation of the power spectral density of the surface profile expressed in terms of the spatial frequency $Sg(\Omega)$ to that in terms of the temporal frequency $Sg(f)$ is through the speed of the vehicle [20-21] :

$$sg\,(f) = \frac{sg\,(\Omega)}{v} \tag{4}$$

By using MATLAB Coding of Road Roughness function in terms of Travel length in a quarter car Model express compared ISO classification of road roughness as PSD function in terms of frequency Hz [11, 25] with constant speed of car as shown in Figure.3.

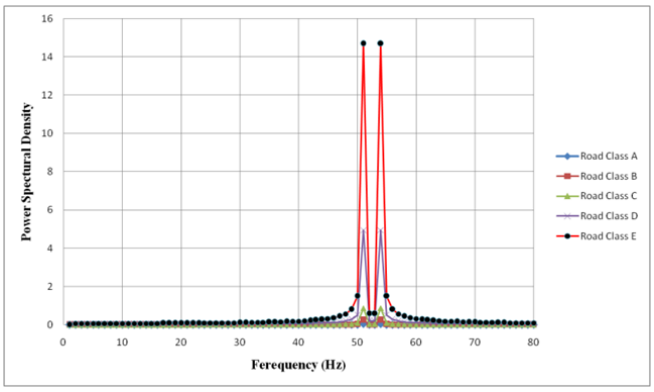

Fig. 3. Compared Road Roughness as PSD function in terms of ferequency Hz in Different Class Road by ISO 2631-1 with Constant Velocity 100 Km/h [22].

3. Finite Element Analysis

In this research, predict fatigue life of suspension components such as wheel hub, suspension arm, pitman arm and package of suspension system, means calculating the number of failure cycles. So for the finite element analysis in software, stress-life method (S-N method) has been used based on the Rain flow cycle counting. A flowchart of the working process in software for the analysis is presented in Fig 4.

3.1. Geometric Modelling

Firstly, the suspension components has been modelled in CATIA modelling software and in the next step, assemble all parts to create package of suspension system as shown in Figure.5.

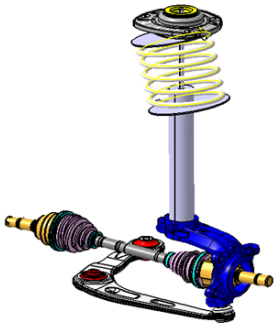

Fig. 4. An image of assemble modelling of package of suspension system in CATIA.

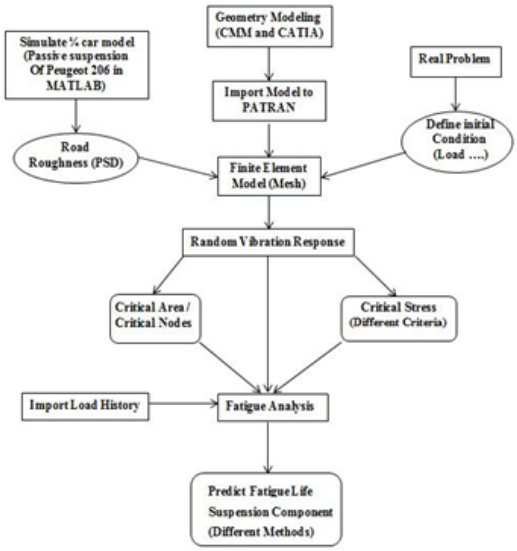

Fig. 5. A flowchart of the working process in software for the finite element analysis of suspension components.

3.2. Material Information

To completely simulate finite element model, information and standards related to the part type provided and considering the constituent materials of the type and determining the part construction operation (casting, good, average and bad machining, polished surface, thermal treatment, etc.) it was applied in the section of materials management in software so that mechanical properties of the part type can be seen in table 2.

Table 2. Mechanical Properties of suspension component [26].

Piece	DIN Standard	Ultimate Stress (MPa)	Yield Stress (MPa)
Wheel hub	20MnCr5	780-1080	540
Pitman Arm	41Cr4	800-950	560
Suspension Arm	31NiCr14	780-930	635
Spring	60SiCr7	1320-1570	1130
Pin	38MnSi4	980-1180	785

3.3. Loading Information

Considering a car moving at the speed of $100Km/h$ and given that the car is moving on a straight road without any changes in the steering column, loading based on the road signals obtained in accordance with the class D road roughness has been applied vertically on the wheel hub located on the pitman arm where can see the fixture and load location on Figure 6.

Fig. 6. Fixture and load location on the assembly suspension model in FEM.

To specify the location of the suspension system is used three-dimensional Cartesian coordinate. Where X-axis is along the length of the vehicle, the y-axis and z-axis along the width and height direction of the vehicle. So, Zero point of coordinate is considered at the contact surface of the wheel and ground. location of other 4-point on the system is as follows :

Location Point 1 : the center point of wheel hub is $(0, 0, +28cm)$.

Location Point 2 : spring is in the $Y - Z$ plane and makes an angle of 15 degrees with Z axis.

Location Point 3 : end point of shaft compared to the initial point has no component along the x-axis. In the Z direction has component value of $27mm$ placed above the wheel hub center.

Location Point 4 : coordinates x and y of middle Bush of triangular suspension arm is exactly located under shaft. On the other hand it is parallel to the axis of the wheel hub center, only in the Z direction ; there is component value of $189mm$ in height. In the other world, is located $91mm$ below of the wheel hub center axis.

In addition, the loading location is shown in the figure 6.

4. Results and Discussion

4.1. Random Vibration Response

The analysis is used to calculate the steady state response of a structure under sinusoidal excitation or generalizable to a sinusoidal excitation with variable amplitude and phase. The most important results obtained from this analysis are : Critical areas and stress, velocities and accelerations in the nodes, forces and stresses on elements.

Since, the analysis is very time-consuming and subsequent fatigue analyses are more time-consuming, it is attempted to choose a proper mesh size by obtaining the extent the mesh size of triangular element Tet10 effects the critical stresses in the suspension system

constituents, and overviewing the results. So it needs less workspace for calculations, and results in a shorter time. Therefore, given different sizes for mesh grading, the information related to the critical stresses in the different parts is reported in table 3.

Table 3. The effect of mesh size on the critical stress in the suspension system according to von Misses criterion.

Model	Size Mesh	Number of Nodes	Number of Elements	Critical Stress (MPa)
Wheel hub	0.1	8017	4394	282
	0.3	7311	4040	283
	1	5352	2902	237
Pitman arm	0.1	17723	35478	369
	0.3	14860	29752	362
	1	9632	19296	348
Suspension arm	0.1	16789	32932	393
	0.3	14524	28466	385
	1	11842	23219	360.5
Package of suspension	0.1	18412	35897	402
	0.3	15621	30437	396
	1	10487	20250	370

In the following, critical stresses of the suspension components caused by random vibrations analysis according to different criteria are presented in Table 4.

Table 4. Critical stress in the suspension's pitman arm according to different criteria.

Model	Criterion	Von Misses	Tresca	Max principle
Wheel hub	Max Stress (MPa)	237	241	247
	Min Stress (MPa)	160	167	168
Pitman arm	Max Stress (MPa)	348	352	367
	Min Stress (MPa)	198.7	211	217
Suspension arm	Max Stress (MPa)	360.5	372	376
	Min Stress (MPa)	240	247	251.3
Package of suspension	Max Stress (MPa)	370.2	385.46	394.9
	Min Stress (MPa)	206.7	218.01	221

4.2. Fatigue Analysis

To predict the fatigue life under random vibration loading in MSC.FATIGUE software, in the first phase of the part random vibration response, it is necessary to determine the critical area in the part, identify the most critical nodes in the part under random vibration loading, and consider maximum critical stress of the part for using in the next step, so that complicated and time consuming fatigue calculations be done on the critical points of the parts' critical areas. Thus, using the analysis in the previous section, critical areas of components are shown in Figures 7-10 for using in fatigue analysis and its fatigue life prediction.

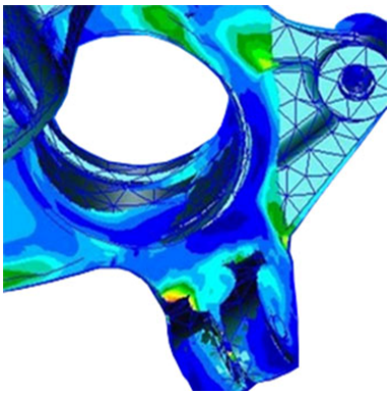

Fig. 7. A stress contour of the critical area of the pitman arm under random vibration loading.

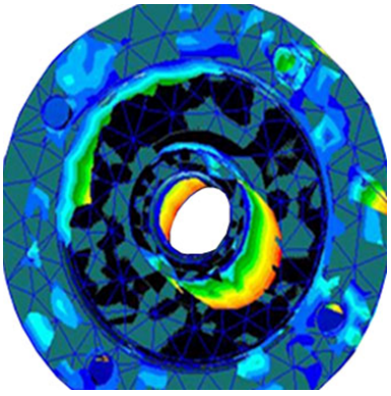

Fig. 8. A stress contour of the critical area of the wheel hub under random vibration loading [23].

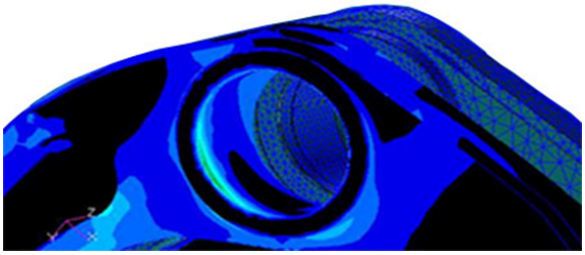

Fig. 9. A stress contour of the critical area of the suspension arm under random vibration loading.

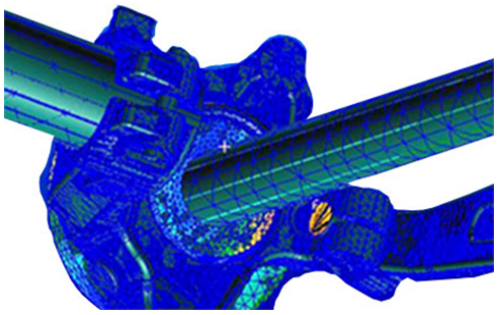

Fig. 10. A stress contour of the critical area of the package of suspension system under random vibration loading.

Then, using two different computational methods for predicting the fatigue life in software (Dirlik and narrow-band), the parts' fatigue life are obtained under loading conditions (car moving at a constant speed in class D road). Finally, given the elapsed time in a loading cycle, determined number of cycles' repetition before failure, and the car's speed, number of loading cycle before failure to the distance travelled by the car in terms of kilometer can be calculated. Therefore, fatigue life of the model has been reported in terms of its function in Table 5 [27-29].

4.2.1. Dirlik Theory

This is one of the best methods that has been subject to modifications. The numerical simulations of the time histories are used for two different spectra. By using a concoction of one exponential and two Rayleigh probability densities, the cycle-amplitude distribution has been approximates (In 1985). The Rain-flow cycle amplitude probability density estimate is given by [30]

$$P_a(s) = \frac{1}{\sqrt{m_0}}\left[\frac{G_1}{Q}e^{\frac{-z}{Q}} + \frac{G_2 Z}{R^2}e^{\frac{-z^2}{2R^2}} + G_3 Z e^{\frac{-z^2}{2}}\right] \tag{5}$$

Where Z is the normalized amplitude and x_m is the mean frequency, as defined by the author of the method [30] :

$$Z = \frac{s}{\sqrt{m_0}} \tag{6}$$

$$x_m = \frac{m_1}{m_0}\left(\frac{m_2}{m_4}\right)^{0.5} \tag{7}$$

And the parameters G_1 to G_3, R and Q are defined as [30] :

$$G_1 = \frac{2\left(x_m - \infty_2^2\right)}{1+\infty_2^2} \tag{8}$$

$$G_2 = \frac{1-\infty_2 - G_1 + G_1^2}{1-R} \tag{9}$$

$$G_3 = 1 - G_1 - G_2 \tag{10}$$

$$R = \frac{\infty_2 - x_m G_1^2}{1 - \alpha_2 - G_1 + G_1^2} \tag{11}$$

$$Q = \frac{1.25\left(\alpha_2 - G_3 - G_2 R\right)}{G_1} \tag{12}$$

While α_2 has already been defined with [30] :

$$\alpha_i = \frac{m_i}{\sqrt{m_0 m_{2i}}} \tag{13}$$

The closed form expression for the fatigue life intensity has been derived in the form [30] :

$$\bar{D}^{DK} = C^{-1}\vartheta_p m_0^{\frac{k}{2}}\left[G_1 Q^k \Gamma\left(1+k\right) + \left(\sqrt{2}\right)^k \Gamma\left(1+\frac{k}{2}\right)\left(G_2\left|R\right|^k + G_3\right)\right] \tag{14}$$

4.2.2. Narrow Band Theory

Miles presented Narrow Band Theory in 1956. There is feasible consider that every peak is congruous with a cycle .as a result, the cycle amplitudes are Rayleigh distributed. Here, there is presented stress amplitudes [30] :

$$\bar{D}^{NB} = \vartheta_0 C^{-1}\left(\sqrt{2m_0}\right)^k \Gamma\left(1+\frac{k}{2}\right) \tag{15}$$

Where ϑ_0 is the expected positive zero crossings intensity, which is very close to the peak intensity ϑ_p.

For a narrow band process, C and k are material fatigue parameters. m_0 is the 0-th spectral moment and $\Gamma(.)$ is the Euler gamma function, which is defined as [30] :

$$\Gamma\left(z\right) = \int_0^\infty t^{z-1} e^{-t} dt \tag{16}$$

Table 5. Fatigue life in terms of kilometres travelled using different computational methods in finite element software.

Component	Dirlik Method	Narrow Band Method	Damaged Part
Wheel hub	116944	111541.7	The outer surface of the inner shaft
Pitman Arm	92638.9	86736.1	The Top right corner of joint in relate to Mounting link
Suspension Arm	46388.9	41388.9	The Internal of Middle rubber Bush
Package of Suspension System	191388.9	157222.2	The Top of Mounting link between pitman arm and suspension arm

5. Conclusion

Nowadays, the suspension systems designers used new technology in advanced vehicles. Studies in different fields of fatigue loading are very significant. Most of the time, it's directly related to the passenger comfort and safety without any warning about fracture time. For actual analysis and results, random vibration is applied for the simulation of the suspension components and assembly of them.

For avoiding of conducting of expensive tests, as well as, easy development of parameters for sensitivity analysis, engineers used finite element method. They can optimize the presented model parametrically.

We can. The research achievements are as follows :

1. The maximum and minimum stress is related to triangular suspension arm and Wheel hub respectively. So, if have a same cyclic loading on all parts of suspension components, the triangular suspension arm is failed. For instance, critical stress of pitman arm in Von Misses criteria was reported to be 348MPa that is less than its yield stress. So, this part will not fail under static loading and should be analyses fatigue phenomena.

2. According to the present study, when the vehicle was derived with a speed constant, 100 km/h, given the loading conditions burdened on the system. if investigate all parts in separate case, after 46388.9 travelled car, can see fatigue phenomena on the triangular suspension arm and the middle rubber bush will be failed and break dawn.

3. Finally, with respect to results, after 191388.9 km driving, failing occur on Mounting link between pitman arm and triangular suspension arm and with analysing of separated from each other, we can have exact inspection.

REFERENCES

[1] Lee. Y.L., Pan. J., Hathaway. R., Sarkey. M., 'Fatigue Testing and Analysis", Handbook of Wiely Publication, (2005).

[2] Stefner. R.I., Fachez. H.A., "Metal Fatigue in Engineering", Guilan University Publication, First Edition, (2000).

[3] Clensin. M., Lokach. P., "Metal Fatigue", Center for Academic Publication, First Edition,(2002).

[4] Elmadany. M.M., "The performance passive car suspension system in Tractor-Semitrailer vehicles", Engineering Science, (1990), Vol. 2, pp. 131-152.

[5] Bishop. N., Steinbeck. J., Sherratt. F., "Finite Element Based Fatigue Calculations", Company of MSC Software, Alzenau Germany, (2005).

[6] Badih. A., Baumann. J., "Design of Formula SAE Suspension", SAE Technical Paper Series, (2002), 01, 3310.

[7] Haiba. M., Barton. D.C., Brooks. P.C., Levesley. M.C., "The development of an optimization algorithm based on fatigue life", International Journal of Fatigue, (2003), Vol. 25, pp. 299-310.

[8] Nadot. Y., Denier. V., "Fatigue failure of suspension arm : experimental analysis and multiaxial criterion", Engineering Failure Analysis, (2004), Vol. 11, pp. 485-499.

[9] Svensson. T., Johannesson. P., Mare. J.D., "Fatigue life prediction based on variable amplitude tests-specific applications", International Journal of Fatigue, (2005), Vol. 27, pp. 966-973.

[10] Buciumeanu. M., Miranda. A.S., Pinho. A.C.M., Silva. F.S., "Design improvement of an automotive-formed suspension component subjected to fretting fatigue", Engineering Failure Analysis, (2007), Vol. 14, pp. 810-821.

[11] Eyvari. A.S., "Analysis of impact incoming to the vehicle on the rough road", 4th National conference of Civil Engineering of Tehran University, (2008).

[12] Martinez. A.G.R., Singh. S.P., Ballester. V.A.C., "Measurement and analysis of vibration levels for truck transport in spain as a function of payload, suspension and speed", Packaging Technology and Science of Wiley Inter Science, (2007).

[13] Colombo. D., Gobbi. M., Mastinu. G., Pennati. M., "Analysis of an unusual McPherson suspension failure", Engineering Failure Analysis, (2009), Vol. 16, pp. 1000-1010.

[14] Borg. L.T., "An approach to using finite element models to predict suspension member loads in a formula SAE vehicle", Master of Science in Mechanical Engineering at Blacksburg university of Virginia, (2009).

[15] Rahman. M.M., Kadirgama. K., Noor. M.M., rejab. M.R.M., "Fatigue life prediction of lower suspension arm using strain-life approach", European Journal of Scientific Research, (2009), Vol. 30, pp. 437-450.

[16] Breytenbach. B., Schalk Els. P., "Optimal vehicle suspension characteristics for increased structural fatigue life", Journal of Terra mechanics, (2011).

[17] Tung. S.L., Juang. Y.T., Lee. W.H., Shieh. W.Y., Wu. W.Y., "Optimization of the exponential stabilization problem in active suspension system using PSO", Expert Systems with Applications, (2011), Vol. 38.

[18] Schwab. H.L., Caffrey. J., Tools. F.E., Lin. J., "Fatigue analysis using random vibration", Ford Motor Company Reports.

[19] Wong. J.Y., "Theory of grounf vehicle book", publication of university Ottawa, Third Edition, (2001).
[20] Mashhadi. B., Hatamabad. M., "Vehicle motion analysis on the test roads in virtual environments", Journal of Automobile Engineering and Related Industries, (2009).
[21] Michae. A., Sek., "a modern technique of transportation simulation for package performance testing", Victoria University of Technology, (1996).
[22] Reza-Kashyzadeh. K., Ostad-Ahmad-Ghorabi. M.J., Arghavan. A., "Investigating the Effect of Road Roughness on Automotive Component", Engineering Failure Analysis, (2014), Vol. 41, pp. 97-108.
[23] Taghizadeh. S.R., "Digital signal processing", University of north London, (2000), Part. 3.
[24] Reza-Kashyzadeh. K., Ostad-Ahmad-Ghorabi. M.J., Arghavan. A., "Fatigue Prediction on Wheel's Hub under Random Vibration Based Road Roughness", Journal of Mechanical Engineering and Vibration, (2013), Vol. 1, Issue. 2.
[25] Ostad-Ahmad-Ghorabi. M.J., Arghavan. A., Reza-Kashyzadeh. K., "investigation effect of velocity on the transfer function values under road roughness", International journal of emerging technology and advanced engineering, (2012), Vol. 2, pp. 9-14.
[26] Jafari. M., Heyhat. M., "Mechanical design by CATIA", Afarang Publication, (2006), Edition.1.
[27] MSC Software Group, "Durability and Fatigue life Analysis Using MSC Fatigue", MSC Software publication, (2008), Vol. 1, PAT318.
[28] MSC Software Group, "Fatigue TM 2005 r2 User's Guide", MSC Software Publication, (2005), Vol. 1.
[29] MSC Software Group, "Fatigue TM 2005 r2 User's Guide", MSC Software Publication, (2005), Vol. 2.
[30] Mrsnik. M., Slavic. J., Boltezar. M., "Frequency Domain Method for a Vibration Fatigue Life estimation-Application to Real Data", International Journal of Fatigue, (2013), Vol. 47.

Biographical notes

Kazem Reza Kashyzadeh, born in 1986, is currently a PhD candidate at Mechanical Engineering of Sharif University and Technology, International Campus, IRAN. His research interests include Fatigue and Fracture.

ISSN : 2335 - 1357

Mediterranean Journal of Modeling and Simulation

Med. J. Model. Simul. 04 (2015) 051-059

Reduction of hot points formation in a heat tube bundle exchanger

Youcef Kamla [a] *, Mohamed Bouzit [a] , Djamel Sahel [a] , Warda Boudaoud [a] , Abdelkader Karas [b]

[a] Université des sciences et de la Technologie - Mohamed Boudiaf - d'Oran BP 1505, El-M'Naouer, Oran 31000, Algérie

[b] Université de Khemis miliana

ARTICLE INFO

Article history :
Received September 2014
Accepted June 2015

Keywords :
Hot points ;
LHTA ;
Heat exchangers ;
Baffles.

ABSTRACT

Among the major problems in the use of baffles in heat exchangers is the formation of hot points due to the stagnation of the flow behind baffles. The present work shows a design of a porous space in the baffles in order to shake the dead zones behind these baffles. The numerical investigation is based on the Navier Stocks averaged (RANS) using FLUENT software. The results validated by experimental data from the literature shows that the porous space presented in this paper reduces in an observable manner the hot points and increase the heat transfer rate.

1. Introduction

Plusieurs installations industrielles ont une charge thermique élevée, des dimensions de plus en plus compliquées et ont besoins toujours d'un rendement élevé, par exemple les échangeurs de chaleurs utilisés pour le refroidissement ou le chauffage des huiles et quelques produits gazeux. Depuis des décennies, les techniques d'augmentation du taux de transfert thermique utilisent des chicanes attachées sur la surface de chauffage afin de fournir une meilleur intensité de transfert thermique et favoriser la turbulence. Mais comme toutes les applications industrielles, les chicanes créent deux problèmes majeurs : les pertes de pression et la formation des points chauds particulièrement derrière les chicanes. Pour la conception des échangeurs de chaleurs où les chicanes jouent le rôle d'un générateur de vortex, la majorité des travaux sont basés sur plusieurs paramètres tels que la forme des chicanes ; par exemple la forme V. [1-6] et la forme W. [7]. Toutes les formes proposées dans ces travaux améliorent le taux de transfert thermique et associent des pertes de pression catastrophiques. L'angle d'attaque prend la particularité par plusieurs

*Email : kamla_youcef@yahoo.fr

auteurs, Dutta et al. [8] ont conclu dans leur travail expérimental que la taille, la position et l'orientation des chicanes influent toutes sur le taux de transfert thermique. Parmi les problèmes majeurs d'insertion de chicanes sur les parois des canaux, la formation des zones à faible taux de transfert thermique (LHTA) et particulièrement derrière les chicanes. Ce problème a été corrigé de manière significative par Liu et al. [9], Jin et al. [10] en introduisant l'utilisation de chicanes perforées.

L'angle d'orientation est aussi un paramètre important qui s'est abordé dans la littérature avec les travaux de Tandiroglu et al. [11]. Ils ont examiné expérimentalement la dissipation d'énergie dans un tube muni de chicanes semi circulaires avec trois angles d'orientation $\beta = 45°$, $90°$, $180°$ et trois rapports d'espacement $H/D = 1$, 2 et 3. Ils ont conclus que la chicane de type 9031 représente un meilleur choix pour un bon transfert thermique. Dans le même travail, Tandiroglu. [12] a présenté des formules empiriques pour les calculs du nombre de Nusselt ainsi que le facteur de frottement. Dans un autre travail, Tandiroglu. [13] a examiné la génération de l'entropie pour les déférents types de chicanes.

L' idée du présent article est une combinaison entre l'angle d'orientation présenté par Tandiroglu. [12] et l'espace perforé utilisé par Liu et al. [9] dans le cadre de la réduction de la formation de zones à faible taux de transfert thermique.

2. Configuration de l'écoulement et formulation mathematique

2.1. Géométrie de tubes et de chicanes

Tandiroglu et al. [11] ont présenté neuf tubes dans leur étude expérimentale. Dans ce travail, on garde toutes les dimensions selon la référence [11] sauf la longueur(L) des tubes qui est égale à $319mm$ à cause de la limitation de moyens informatiques disponibles. Le diamètre des tubes (D) est égale à $31mm$. Le rapport de diamètre (H/D) est égale à 1, 2,3 où H est l'espacement entre deux chicanes successives. L'angle d'orientation de chicanes(β) est égale à $45°$, $90°$ et $180°$.

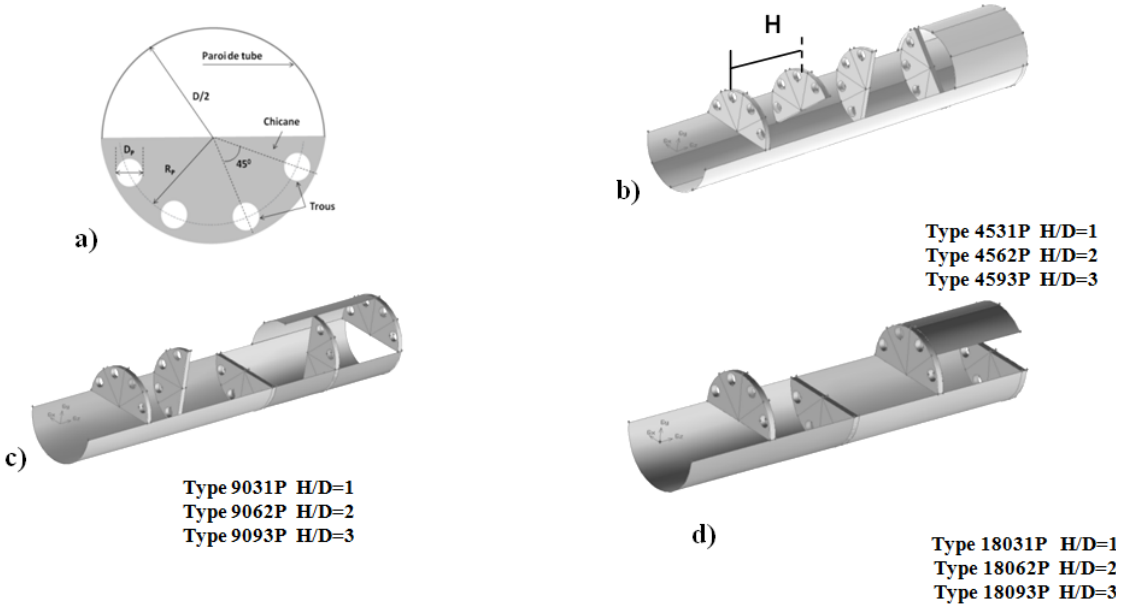

Fig. 1. Géométrie de chicanes après la perforation.

L'intérêt de ce travail est de proposer un espace perforé par quatre trous dans ces chicanes de manière à ce que le fluide de fonctionnement (air) passe par ces trous et agite les zones stagnées derrière les chicanes. La Figure 1.a montre la position des trous sur la chicane, où D_P étant le diamètre des trous ($D_P/D = 0,129$), R_P est le rayon formé par le périmètre qui passe par les trous et l'axe de tube ($R_P/D = 0,419$), et l'angle de 45° montré sur la Figure 1.a représente le décalage angulaire entre les trous. Cette conception peut augmenter l'exécution de transfert thermique en réduisant la formation des zones à faible taux de transfert thermique. La Figure 1.b, c et d nous donne une vue générale sur la forme des chicanes après la perforation.

2.2. Modèle mathématique

Les équations gouvernantes sont les équations de RANS (Reynolds averaged Navier–Stokes) et l'équation d'énergie.

L'équation de continuité :

$$\frac{\partial}{\partial x_i}\left(\rho u_i\right) = 0 \tag{1}$$

L'équation de conservation de mouvement :

$$\frac{\partial}{\partial x_i}\left(\rho u_i u_j\right) = \frac{\partial}{\rho x_i}\left[\mu\left(\frac{\partial u_i}{\partial x_j}\right) - \overline{\rho u_i u_j}\right] - \frac{\partial p}{\partial x_i} \tag{2}$$

Où : $u\prime$ est la fluctuation moyenne de la vitesse.

Equation d'énergie

$$\frac{\partial}{\partial x_i}\left(\rho u_i T\right) = \frac{\partial}{\partial x_j}\left(\left(\Gamma + \Gamma_t\right)\frac{\partial T}{\partial x_j}\right) \tag{3}$$

Où : Γ est la diffusivité thermique moléculaire, donnée par $\Gamma = \mu/pr$, Γ_t est la diffusivité thermique turbulente, donnée par $\Gamma_t = \mu_t/pr_t - \overline{\rho u_i u_j}$. Sont les contraintes de Reynolds calculées par l'hypothèse de Boussinesq. Pour la fermeture de système on base sur le modèle de turbulence $k - \varepsilon$ réalisable.

Le Coefficient de frottement f est calculé par la chute de pression ΔP à travers le tube :

$$f = \frac{2}{(L/D_h)}\frac{\Delta p}{\rho U^2} \tag{4}$$

L'étude du comportement thermique des chicanes basées sur le nombre de Nusselt local, est donné par :

$$Nu_{(x)} = \frac{h_{(x)} D_h}{(k_f)} \tag{5}$$

Où $h(x)$ étant le coefficient d'échange thermique.

Et le nombre de Nusselt moyen :

$$Nu_{(x)} = \frac{1}{A}\int Nu_{(x)}\partial A \tag{6}$$

Le coefficient de performance η est donné par :

$$\eta = (Nu/Nu_0)/(f/f_0)^{1/3} \tag{7}$$

2.3. Condition aux limites

A l'entrée du canal, la température d'admission de l'air est égale à $300°K$ ($P_r = 0.71$). Les propriétés physiques de l'air sont constantes. La condition de non-glissent est mise en application sur les parois des tubes. La température des parois est constante, est maintenue à $350°K$.

2.4. Procédure numérique

La méthode de volumes finis utilisé dans ce travail basée sur l'algorithme SIMPLE. Le maillage non structuré générés sur les domaines de calculs est de type tétraédrique a été examinées par le solveur FLUENT. Une séries de maillages a été effectuée à l'aide de pro-processeur Gambit 2.3.16 afin de choisir approximativement 660000 éléments qui représente des résultats stables pour les différents domaines. Le FLUENT est utilisé pour calcule de l'écoulement de fluide et de transfert thermique. Les termes convectifs dans les équations régissantes sont discrétisées par le schéma de premier ordre. Les facteurs de sous-relaxation sont sélectionnées par défaut du solveur utilisé. Le critère de convergence des résiduels sont ; $10-3$ pour les équations d'écoulement et $10-6$ pour l'équation d'énergie.

3. Comparaison de résultats

Les Figures 2 et 3 représentent une comparaison entre les résultats de présent travail effectuées sur un tube lisse et des formules empiriques de nombre de Nusselt et le coefficient de frottement. On résume ces résultats sur le tableau suivant :

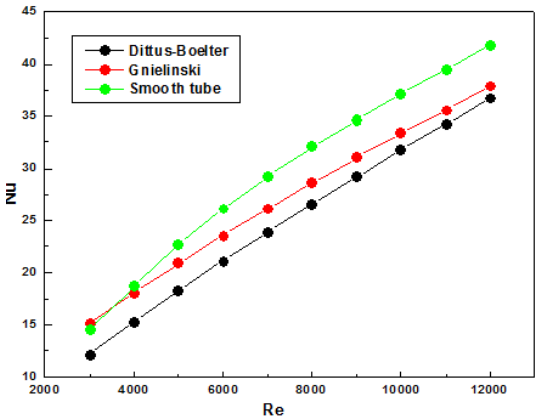

Fig. 2. Comparaison des résultats de nombre de Nusselt.

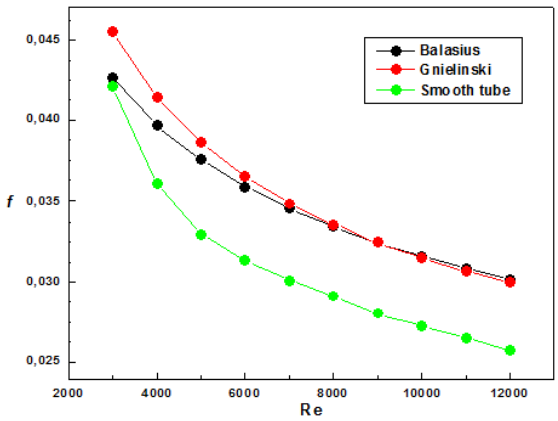

Fig. 3. Comparaison des résultats de coefficient de frottement.

Table 1. Comparaison de résultats.

Nombre de Nusselt Nu		Coefficient de frottement f	
Dittus-Boelter	Gnielinski	Balasius	Gnielinski
±12.4%	±10%	±14.1%	±13.3%

Corrélation de Dittus-Boelter :

$$Nu = 0.023\mathrm{Re}^{0.8}\,\mathrm{Pr}^{0.4} Pour\ \mathrm{Re} \geq 10000 \tag{8}$$

Corrélation de Gnielinski :

$$Nu = [(f/8)]\,\mathrm{Re}\,\mathrm{Pr}/\left[1 + 27\,(f/8)^{1/2}\left(\mathrm{Pr}^{2/3} - 1\right)\right]\ \ Pour\ 2300 \leq \mathrm{Re} \leq 5 \cdot 10^6 \tag{9}$$

Corrélation de coefficient de frottement d'après le diagramme de Moody :

$$f = 0.316\mathrm{Re}^{-0.25}\ Pour\ \mathrm{Re} \leq 2 \cdot 10^4 \tag{10}$$

Corrélation de Gnielinski :

$$f = (0.79\ln\mathrm{Re} - 1.64)\ \ Pour\ 2300 \leq \mathrm{Re} \leq 5 \cdot 10^6 \tag{11}$$

4. Résultats et discussions

4.1. Points chauds et le transfert thermique

Les zones à faible taux de transfert thermique dues à la formation des zones de recirculation à très faible vitesse. Ces dernier créent les points chauds (où LHTA).

Liu et *al.* [9] basent sur le nombre de nusselt pour détecter les zones à faible taux de transfert thermique (LHTA).

Dans ce travail on se base sur la température maximale de la paroi pour détecter les canaux chicanés à forte ou moin forte formation de points chauds.

La Fig 5 représente la vartiation de la température maximale de la paroi en fonction de l'angle d'orientation de chicane β pour les nombre de Renolds 3000, 6000, 9000,12000. La Figure 4 montre la distribution des points chauds sur la paroi pour $H/D = 1$, $\beta = 45°$, 90° et 180°. Ces Figs. montrent les phenomènes suivants :

– La temperature maximale de la paroi diminue suivant l'augmentation du nombre de Reynolds. Alors l'augmentation de nombre de reynolds diminue la formation des points chauds.

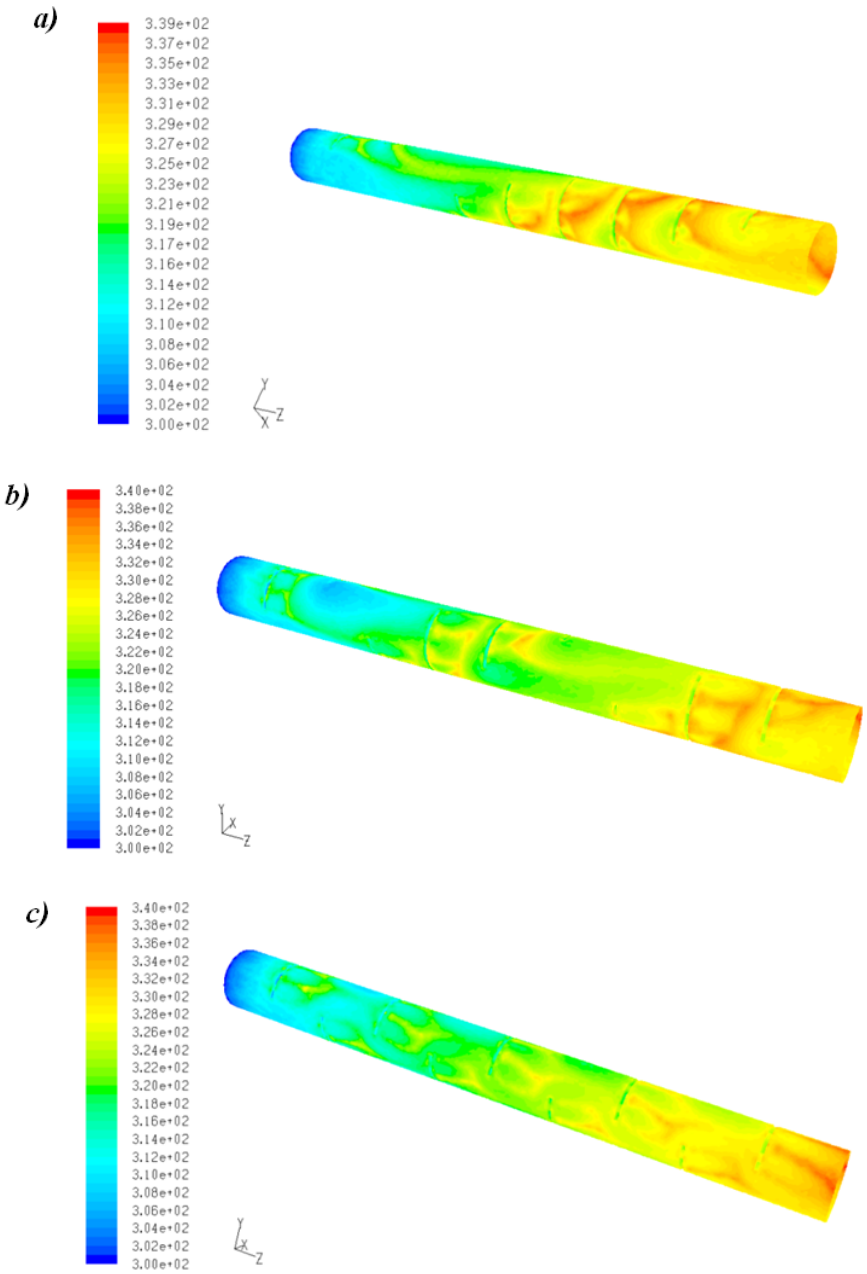

Fig. 4. Distribution des points chauds sur les parois :a) β=45°, b) β=90°, c) β=180°,(H/D=1, Re=12000).

– Généralement, le rapport de diametre $H/D = 1$ pour tous les cas , la température maximale de la paroi est moindre par comparaison avec les cas de $H/D = 2$ et 3, donc $H/D = 1$ est le meuilleur choix pour la formation des points chauds.
– Généralement, l'angle d'orientation de chicane $\beta = 180°$, represente le meuilleur choix parce que $T_w\ (max)$ est toujours petite par rapport aux autes cas.

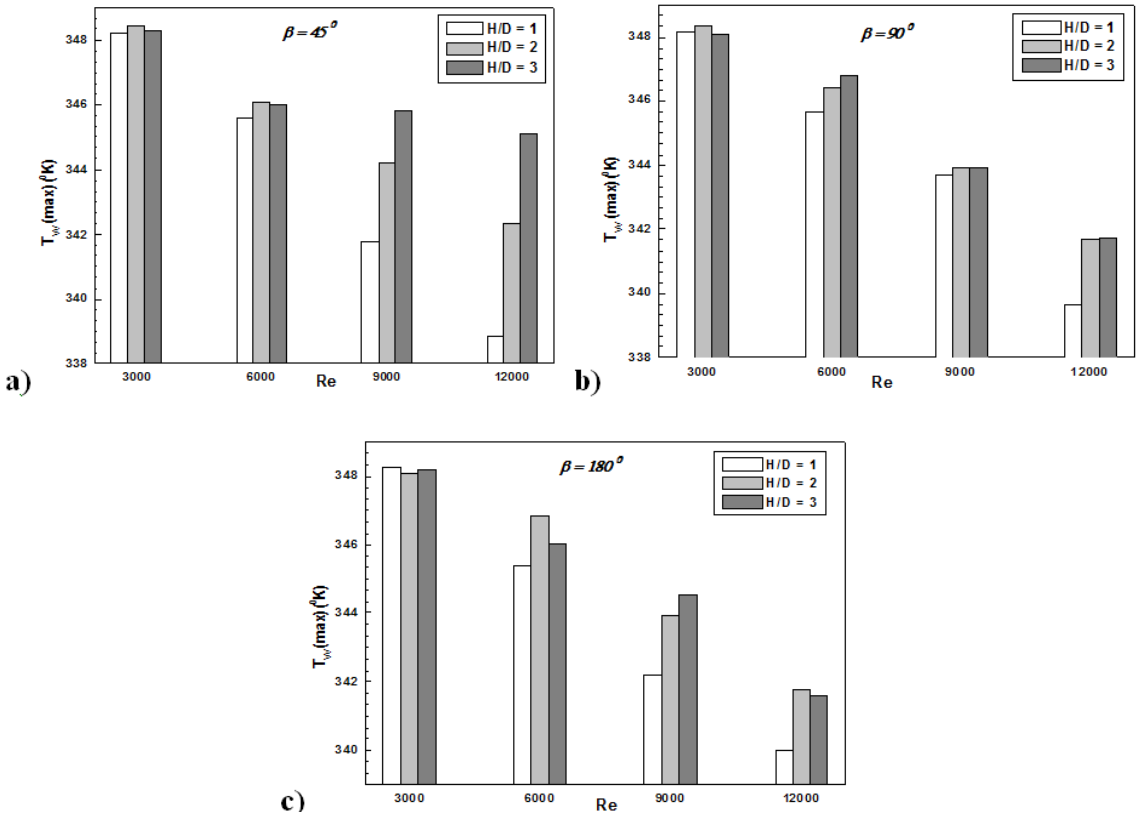

Fig. 5. Variation de la température maximale de la paroi en fonction de Re, β et H/D.

La Figure 6 représente la variation de nombre de Nusselt en fonction du nombre de Reynolds. Elle montre que l'angle d'orientation 45° représente le mauvais choix pour l'exécution du transfert thermique. Dans cette figure le type 18031P représente un meilleur taux de transfert thermique d'environ de 130 à 400 % par rapport au tube lisse.

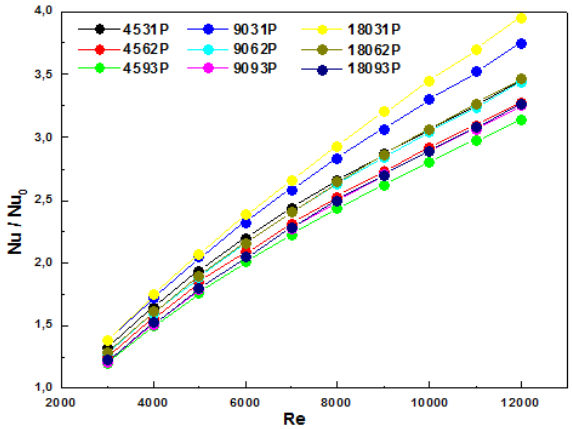

Fig. 6. Variation du nombre de Nusselt en fonction des nombres de Reynolds.

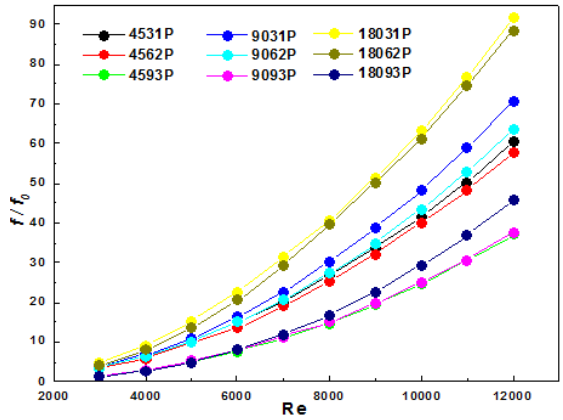

Fig. 7. Variation du coefficient de frottement en fonction des nombres de Reynolds.

4.2. Pertes de pression

Comme tous les travaux proposés dans la littérature, les géométries étudiées dans ce travail posent le problème de pertes par frottement. La Figure 7 représente la variation de perte par frottement en fonction de nombres de Reynolds. Cette figure montre que l'angle d'orientation 90° représente un minimum de pertes par frottement et le type 18031P assure maximum valeurs de coefficient de frottement d'environ de 5 à 90 fois par rapport au tube lisse. La Figure 8 illustre la variation de coefficient de performance thermique en fonction de nombres de Reynolds. Cette figure montre que le coefficient de performance thermique déminu en fonction de Re dans les cas de rapport d'espacement $H/D = 3$. Le type 18093 assure maximum facteur de performance thermique environ de 1.15.

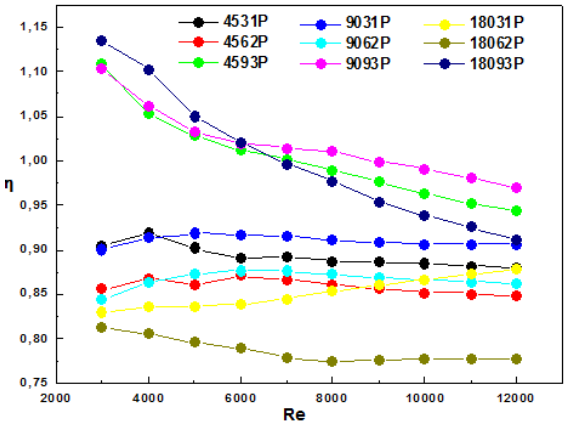

Fig. 8. Variation du coefficient de performance thermique en fonction des nombres de Reynolds.

5. Conclusions

Une investigation numérique a été effectuées dans ce travail pour examiner le comportement thermique et dynamique de l'écoulement turbulent dans un tube circulaire muni de chicanes semi-circulaires et perforées. Les résultats numériques montrent que l'angle d'orientation et l'espacement des chicanes influent directement sur l'exécution du transfert thermique par la diminution de formation des points chauds et les pertes par frottement. Particulièrement ces résultats représentent la chicane de type 18031P comme

meilleur choix dans le phénomène de transfert de chaleur car ce dernière assure un meilleur taux de transfert thermique d'environ de 130-400%, par conséquence cette augmentation associe une perte de pression de 5 à 90 fois par comparaison au tubes lisses.

REFERENCES

[1] Dong H. L., Dong-Ho R., Kyung M. K., Hyung H. C., Hee K. M. 2009. Detailed measurement of heat/mass transfer with continuous and multiple V-shaped ribs in rectangular channel. Energy 34, pp.1770–1778.

[2] Wei P., Pei-Xue J., Yang-Ping W., Bing-Yuan W. 2011. Experimental and numerical investigation of convection heat transfer in channels with different types of ribs. Applied Thermal Engineering 31, pp. 2702-2708.

[3] Pongjet P., Wayo C., Sutapat K., Chinaruk T., 2011. Numerical heat transfer study of turbulent square-duct flow through inline V-shaped discrete ribs. International Communications in Heat and Mass Transfer 38, pp. 1392–1399.

[4] Pongjet P., Withada J., Sutapat K., Chinaruk T., 2012. 3D simulation of laminar flow and heat transfer in V-baffled square channel. International Communications in Heat and Mass Transfer 39, pp. 85–93.

[5] Hans V.S., Saini R.P., Saini J.S., 2010. Heat transfer and friction factor correlations for a solar air heater duct roughened artificially with multiple v-ribs. Solar Energy 84, pp. 898–911.

[6] Sukhmeet S., Subhash C., Saini J.S., 2012. Exergy based analysis of solar air heater having discrete V-down rib roughness on absorber plate. Energy 37, pp. 749-758.

[7] Atul Lanjewar J.L., Bhagoria R.M., Sarviya., 2011. Heat transfer and friction in solar air heater duct with W-shaped rib roughness on absorber plate. Energy 36, pp. 4531-4541.

[8] Prashanta D., Akram H., 2005. Internal cooling augmentation in rectangular channel using two inclined baffles. International Journal of Heat and Fluid Flow 26, pp. 223–232.

[9] Huichun L., Jianhua W., 2011. Numerical investigation on synthetical performances of fluid flow and heat transfer of semiattached rib-channels, International Journal of Heat and Mass Transfer 54, pp. 575–583.

[10] Qiang J., Songlin L., Min Li., Weihua W., 2012. Numerical Investigation of heat transfer enhancement in ribbed channel for the first wall of DFLL-TBM in ITER, Fusion Engineering and Design-Article in Press.

[11] Ahmet T. , Teoman A., 2006. Energy dissipation analysis of transient heat transfer for turbulent flow in a circular tube with baffle inserts. Applied Thermal Engineering 26, pp. 178–185.

[12] Ahmet T., 2006. Effect of flow geometry parameters on transient heat transfer for turbulent flow in a circular tube with baffle inserts. International Journal of Heat and Mass Transfer 49, pp. 1559–1567.

[13] Ahmet T., 2007. Effect of flow geometry parameters on transient entropy generation for turbulent flow in circular tube with baffle inserts. Energy Conversion and Management 48, pp. 898–906.

ISSN : 2335 - 1357

Mediterranean Journal of Modeling and Simulation

Med. J. Model. Simul. 04 (2015) 060-072

New exact bound states solutions for (C.F.P.S.) potential in the case of non commutative three dimensional non relativistic quantum mechanics

Abdelmadjid MAIRECHE [a] *,

[a] Physics department, Sciences Faculty, University of M'sila-Algeria.

ARTICLE INFO

Article history :
Received March 2015
Accepted June 2015

Keywords :
Schrödinger equation ;
Hydrogen atom ;
Star product ;
Noncommutative space ;
Central fraction power singular potential.

ABSTRACT

We obtain here the modified bound-states solutions for central fraction power singular potential (C.F.P.S.) in noncommutative 3-dimensional non relativistic quantum mechanics (NC-3D NRQM). It has been observed that the commutative energy spectra was changed, and replaced degenerate new states, depending on four quantum numbers : j, l and $s_z = \pm 1/2$ corresponding to the two spins states of electron by (up and down) and the deformed Hamiltonian formed by two new operators : the first describes the spin-orbit interaction , while the second obtained Hamiltonian describes the modified Zeeman effect (containing ordinary Zeeman effect) in addition to the usual commutative Hamiltonian. We showed that the isotropic commutative Hamiltonian H_{CFPS} will be in non commutative space anisotropic Hamiltonian $H_{NC-CFPS}$.

1. Introduction

Recently a considerable effort has been devoted to the study of physics phenomena on commutative and noncommutative space-times ; the study of central physical problems has attracted much attention. The fraction power singular potential and fraction power potential are two exactly solvable like the Columbian and harmonic oscillator in quantum mechanics in two and three dimensional space [1-31]. The central fraction power singular potential has been successfully used in particle physics phenomenology and may be useful in other physics problems [30, 31]. A new concept of space-time, known by noncommutative spaces, represents a hope to obtain a new and profound interpretation at microscopic scales. In this noncommutative space, we extend the standard rules of quantum mechanics to the generalized Heisenberg relation of uncertainty. The formalism of star product, Boopp's shift method and the Seiberg-Witten map were played fundamental roles in this new theory.

*Email : abmaireche@gmail.com

The rich mathematical structure of the noncommutative theory will lead to get a better understanding of physics phenomena at small distances and hopefully will solve above mentioned problems. The physical idea of a noncommutative space will be satisfied by new mathematical product which replaces the old ordinary product by star product between two arbitrary functions $f(x)$ and $g(x)$ noted by $(*)$, the effect of star product change the ordinary product by $\delta\left(f\left(x\right).g\left(x\right)\right)$ [9- 27] :

$$\delta\left(f\left(x\right).g\left(x\right)\right)=-\frac{i}{2}\theta^{ij}\left(\partial_{i}f\left(x\right)\right)\left(\partial_{j}g\left(x\right)\right) \tag{1}$$

The parameters θ_{ij} are an antisymmetric real matrix of dimension square length in the noncommutative canonical-type space. This paper is organized as follows : in the next section we present the central fraction power singular potential in the commutative three dimensional spaces. In section 3 we study the Hydrogen atom with central fraction power singular potential in (NC-3D NRQM) ; we apply the perturbation theory to deduce the energy levels of electron with two polarizations up and down, also we derive the deformed Hamiltonian of Hydrogen atom with studied potential (C.F.P.S.). The conclusions are given in the last section.

2. The (C.F.P.S.) potential in commutative three dimensional NRQM

The stationary reduced Schrödinger equation with central fraction power singular potential depending only on the distance r leads to the following equation for the radial part of wave equation [31] :

$$\frac{1}{r^{2}}\frac{d}{dr}\left(r^{2}\frac{dR\left(r\right)}{dr}\right)-\frac{l\left(l+1\right)}{r^{2}}R\left(r\right)+\left(E-\alpha r^{\frac{2}{3}}-\beta r^{-\frac{2}{3}}-\gamma r^{-\frac{4}{3}}\right)R\left(r\right)=0 \tag{2}$$

Where E and (α, β and γ) are the energy spectra and three real numbers, respectively. The wave equation $R\left(r\right)$ has the following ansatz [31] :

$$R\left(r\right)=\exp\left(\frac{3}{4}ar^{\frac{4}{3}}+\frac{3}{2}br^{\frac{2}{3}}\right)\sum_{n=0}a_{n}r^{2n/3-\nu} \tag{3}$$

Where a, b and v are three constants :

$$\begin{array}{ll} a= & -\sqrt{\alpha} \\ b= & \frac{E}{2\sqrt{\alpha}} \\ \nu= & l \end{array} \tag{4}$$

The values $v=l$ assure finite values of $R(r)$ at $r=0$, the energy eigenvalues E_{p}^{l} which corresponded $a_{p}\neq0$ and $a_{p+1}=a_{p+2}=\cdots=0$ is given by [31] :

$$E_{p}^{l}=\pm\sqrt{4\alpha}\left\{\left(\frac{4p}{3}+2l+\frac{7}{3}\right)\sqrt{\alpha}+\beta\right\}^{\frac{1}{2}} \tag{5}$$

The various solutions generalized for $p=0$ and $p=1$ are determined from the projection of two equations, respectively [31] :

$$\begin{array}{l}\Psi^{0}_{l,m}(r,\,\theta,\,\phi)=\exp\left(-\frac{3}{4}\sqrt{\alpha}r^{\frac{4}{3}}+\frac{3}{4}\frac{E^{l}_{0}}{\sqrt{\alpha}}r^{\frac{2}{3}}\right)\,a_{0}r^{l}Y_{l,m}(\theta,\,\phi)\\ E^{l}_{0}=\pm\sqrt{4\alpha}\left\{\left(2l+\frac{7}{3}\right)\,\sqrt{\alpha}+\beta\right\}^{\frac{1}{2}}\\ \Psi^{1}_{l,m}(r,\,\theta,\,\phi)=\exp\left(-\frac{3}{4}\sqrt{\alpha}r^{\frac{4}{3}}+\frac{3}{4}\frac{E^{l}_{1}}{\sqrt{\alpha}}r^{\frac{2}{3}}\right)\,r^{l}\left(a_{0}+a_{1}r^{\frac{2}{3}}\right)\,Y_{l,m}(\theta,\,\phi)\\ E^{l}_{1}=\pm\sqrt{4\alpha}\left\{\left(2l+\frac{11}{3}\right)\,\sqrt{\alpha}+\beta\right\}^{\frac{1}{2}}\end{array}\tag{6}$$

The natural unites ($c=\hbar=2m=1$) and ($\mu=s$) throughout this paper.

3. The (C.F.P.S.) potential in NC 3D NRQM

3.1. Noncommutative (C.F.P.S.) Hamiltonian

The first equation for star-product permits us to deduce the star deformed commutators $\left[x'_{i},^{*}x'_{j}\right]$:

$$\left[x'_{i},^{*}x'_{j}\right]=i\theta_{ij}\tag{7}$$

The deformed Hamiltonian operator $H_{NC-CFPS}$ associated with central fraction power singular potential in NC space, will be determined by the following equation :

$$H_{NC-CFPS}=\frac{\overset{\longleftrightarrow}{p}^{2}}{2m_{0}}+V_{NC-CFPS}(r')\tag{8}$$

Where $V_{NC-CFPS}(r')$ is the operator of the central fraction power singular potential in NC 3D NRQM. We apply the Boopp's shift method ; we deduce the deformed Schrödinger equation with the (central fraction singular power) potential [22-27] :

$$\left(-\frac{\Delta}{2m_{0}}+V_{NC\_CFPS}(r')\right)\,\Psi(\overset{\longleftrightarrow}{r})=E_{NC-CFPS}\Psi(\overset{\longleftrightarrow}{r})\tag{9}$$

Here $E_{NC-CFPS}$ is the energy and $V_{NC\_CFPS}(r')$ is the new potential as a function of operator :

$$V_{NC\_CFPS}(r')=\alpha r'^{\frac{2}{3}}+\beta r'^{-\frac{2}{3}}+\gamma r'^{-\frac{4}{3}}\tag{10}$$

On based to the formulations of the Boopp's shift, the scalar function $(\frac{1}{r})$ can be written in the noncommutative three dimensional spaces as [14,21-26] :

$$\frac{1}{r'}=\frac{1}{r}+\frac{\mathbf{L}\boldsymbol{\theta}}{4r^{3}}\tag{11}$$

Where **L** is the angular momentum, which allows to obtaining after a straightforward calculation :

$$\begin{aligned} \alpha r'^{\frac{2}{3}} &= \alpha r^{\frac{2}{3}} - \frac{\alpha \mathbf{L}\boldsymbol{\theta}}{6r^{\frac{4}{3}}} \\ \beta r'^{-\frac{2}{3}} &= \beta r^{-\frac{2}{3}} + \frac{\beta \mathbf{L}\boldsymbol{\theta}}{6r^{\frac{8}{3}}} \\ \gamma r'^{-\frac{4}{3}} &= \gamma r^{-\frac{4}{3}} + \frac{\gamma \mathbf{L}\boldsymbol{\theta}}{3r^{\frac{5}{2}}} \end{aligned} \tag{12}$$

Inserting Eq. (12) into Eq. (10), one obtains :

$$V_{NC\_CFPS}(r') = V_{C\_CFPS}(r) + V_{CFPS\_P}(r) \tag{13}$$

The term $V_{C\_CFPS}(r)$ represents the usual commutative ordinary potential and the supplementary term $V_{CFPS\_P}(r)$ takes the form :

$$V_{CFPS\_P}(r) = \left(-\frac{\alpha}{6r^{\frac{4}{3}}} + \frac{\beta}{6r^{\frac{8}{3}}} + \frac{\gamma}{3r^{\frac{5}{2}}}\right) \mathbf{L}\boldsymbol{\theta} \tag{14}$$

Where $\boldsymbol{\theta} = \mathbf{2}\boldsymbol{\alpha}'\mathbf{S}$, $\boldsymbol{\alpha}'$ is infinitesimal scalar parameter and **s** is the spin momentum, then, the new NC Hamiltonian $H_{NC-CFPS}$ will be written as follows :

$$H_{NC\_CFPS} = H_{CFPS} + V_{CFPS\_P}(r) \tag{15}$$

Where H_{CFPS} represent the usual Hamiltonian in ordinary commutative space :

$$H_{CFPS} = -\frac{\Delta}{2m_0} + \alpha r^{\frac{2}{3}} + \beta r^{-\frac{2}{3}} + \gamma r^{-\frac{4}{3}} \tag{16}$$

Considering the noncommutativity as a small perturbation on the structure of the coordinate space, the real parameter θ is taken very small and our calculations are taken up to the first order in θ. The new added part $V_{CFPS\_P}(r)$ is proportional with the small non-commutative parameter θ, which as a perturbative term. Furthermore, we can rewrite it to the equivalent physical form :

$$V_{CFPS\_P}(r) = 2\alpha' g(r)\ \mathbf{SL} \tag{17}$$

Where the scalar function $g(r)$ is given by :

$$g(r) = -\frac{\alpha}{6r^{\frac{4}{3}}} + \frac{\beta}{6r^{\frac{8}{3}}} + \frac{\gamma}{3r^{\frac{5}{2}}} \tag{18}$$

This allows write the perturbative term $V_{CFPS\_P}(r)$ as :

$$V_{CFPS\_P}(r) = \alpha' g(r) \left(\mathbf{J}^2 - \mathbf{L}^2 - \mathbf{S}^2\right) \tag{19}$$

Where $\mathbf{J}$ denote to the total momentum. The operator $g(r)$ $\mathbf{SL}$ traduces physically the coupling between spin and orbital momentum. Then, the corresponding NC Hamiltonian $H_{NCCFPS-1}$ will be :

$$H_{NCCFPS-1} = -\frac{\nabla^2}{2m_0} + V_{CFPS}(r) + \theta\left(-\frac{\alpha}{6r^{\frac{4}{3}}} + \frac{\beta}{6r^{\frac{8}{3}}} + \frac{\gamma}{3r^{\frac{5}{2}}}\right)\left(J^2 - L^2 - S^2\right) \tag{20}$$

After a straightforward calculation, we can show that the radial part $R(r)$ of the Schrödinger equation for a solved quantum bound state problem in NC spaces is given by :

$$\begin{array}{l} \frac{1}{r^2}\frac{d}{dr}\left(r^2\frac{dR(r)}{dr}\right) - \frac{l(l+1)}{r^2}R(r) + \\ \left(E - \alpha r^{\frac{2}{3}} - \beta r^{-\frac{2}{3}} - \gamma r^{-\frac{4}{3}} - \left(-\frac{\alpha}{6r^{\frac{4}{3}}} + \frac{\beta}{6r^{\frac{8}{3}}} + \frac{\gamma}{3r^{\frac{5}{2}}}\right) L\theta\right) R(r) = 0 \end{array} \tag{21}$$

We know in non relativistic quantum mechanics the triplets (L_x, L_y, L_z) constructs symmetry generators satisfying the Lie algebra and, therefore, ($\mathbf{J}^2$, $\mathbf{L}^2$, $\mathbf{L}^2$ and J_z) is complete set of observables. Then the combined operator $(\mathbf{J}^2 - \mathbf{L}^2 - \mathbf{S}^2)$ will have two eigenvalues $L_U\left(l,\, j = l + \frac{1}{2},\, s\right)$ and $L_D\left(l,\, j = l - \frac{1}{2},\, s\right)$ corresponding (spin up : $j = l + \frac{1}{2}$) and (spin down : $j = l - \frac{1}{2}$), respectively :

$$\begin{array}{ll} L_U\left(l,\, j = l + \frac{1}{2},\, s\right) = & \left(l + \frac{1}{2}\right)\left(l + \frac{3}{2}\right) - l(l+1) - \frac{3}{4} \\ L_D\left(l,\, j = l - \frac{1}{2},\, s\right) = & \left(l - \frac{1}{2}\right)\left(l + \frac{1}{2}\right) - l(l+1) - \frac{3}{4} \end{array} \tag{22}$$

Then, we can form a diagonal matrix of order (3×3) : $H_{NCCFPS-1}$ with diagonal elements $(H_{NC-CFPS})_{11}$, $(H_{NC-CFPS})_{22}$ and $(H_{NC-CFPS})_{33}$:

$$\begin{array}{l} (H_{NC-CFPS})_{11} = -\frac{\Delta}{2m_0} + V_{CFPS}(r) + \theta g(r)\; L_U\left(l,\, j = l + \frac{1}{2},\, s\right) \text{ for } : j = l + \frac{1}{2} \Rightarrow \text{spinup} \\ (H_{NC-CFPS})_{22} = -\frac{\Delta}{2m_0} + V_{CFPS}(r) + \theta g(r)) L_D\left(l,\, j = l - \frac{1}{2},\, s\right) \text{ for } : j = l - \frac{1}{2} \Rightarrow \text{spindown} \\ (H_{NC-CFPS})_{33} = 0 \end{array} \tag{23}$$

The exact non commutative energies for states : E_{NU} and E_{ND} of an electron with spin up and spin down are determined to be, respectively :

$$\begin{array}{ll} E_{NU} = & E_{p-CFPS} + E_U \\ E_{ND} = & E_{p-CFPS} + E_D \end{array} \tag{24}$$

Where E_U and E_D are the modifications to the energy levels, associated with spin up and spin down. At the first order of parameter θ and by applying the perturbation theory, E_U and E_D became, respectively :

$$\begin{cases} E_U = \alpha' L_U \left(l,\, j = l + \frac{1}{2},\, s\right) \int \Psi^{(p)*}(\overleftrightarrow{r}) g\left(r\right)\, \Psi^{(p)}\left(\overleftrightarrow{r}\right)\, d\tau \\ E_D = \alpha' L_D \left(l,\, j = l - \frac{1}{2},\, s\right) \int \Psi^{(p)*}\left(\overleftrightarrow{r}\right)\, g\left(r\right)\, \Psi^{(p)}\left(\overleftrightarrow{r}\right)\, d\tau \end{cases} \tag{25}$$

Where $d\tau = r^2 \sin(\theta) d\theta d\varphi dr$ denote to the elementary volumes element in spherical coordinates.

3.2. The noncommutative spectra for $p = 0$ for NRQM (C.F.P.S.) potential

The non-commutative modifications of the energy levels, associated with spin up and spin down, in the first order of corresponding $p = 0$ (E_{0U} and E_{0D}), are determined using eqs. (6), (18) and (25) to obtain :

$$\begin{aligned} E_{0U} = &\ \theta' \alpha L_U \left(l,\, j = l - \tfrac{1}{2},\, s\right) \int_0^{+\infty} \left[\exp\left(-\tfrac{3}{4}\sqrt{\alpha} r^{\frac{4}{3}} + \tfrac{3}{4}\tfrac{E_0^l}{\sqrt{\alpha}} r^{\frac{2}{3}}\right)\, a_0 r^l\right]^2 g\left(r\right)\, r^2 dr \\ E_{0D} = &\ \theta' \beta L_D \left(l,\, j = l - \tfrac{1}{2},\, s\right) \int_0^{+\infty} \left[\exp\left(-\tfrac{3}{4}\sqrt{\alpha} r^{\frac{4}{3}} + \tfrac{3}{4}\tfrac{E_0^l}{\sqrt{\alpha}} r^{\frac{2}{3}}\right)\, a_0 r^l\right]^2 g\left(r\right)\, r^2 dr \end{aligned} \tag{26}$$

Which the equations :

$$\begin{aligned} E_{0U} = &\ \theta' \alpha L_U \left(l,\, j = l + \tfrac{1}{2},\, s\right)\, a_0^2 \int_0^{+\infty} \exp\left(-\tfrac{3}{2}\sqrt{\alpha} r^{\frac{4}{3}} + \tfrac{3}{2}\tfrac{E_0^l}{\sqrt{\alpha}} r^{\frac{2}{3}}\right) \\ &\left(-\tfrac{\alpha r^{2l+2-\frac{4}{3}}}{6} + \tfrac{\beta r^{2l+2-\frac{8}{3}}}{6} + \tfrac{\gamma r^{2l+2-\frac{5}{2}}}{3}\right) dr \\ E_{0D} = &\ \theta' \beta L_D \left(l,\, j = l - \tfrac{1}{2},\, s\right)\, a_0^2 \int_0^{+\infty} \exp\left(-\tfrac{3}{2}\sqrt{\alpha} r^{\frac{4}{3}} + \tfrac{3}{2}\tfrac{E_0^l}{\sqrt{\alpha}} r^{\frac{2}{3}}\right) \\ &\left(-\tfrac{\alpha r^{2l+2\frac{4}{3}}}{6} + \tfrac{\beta r^{2l+2-\frac{8}{3}}}{6} + \tfrac{\gamma r^{2l+2-\frac{5}{2}}}{3}\right) dr \end{aligned} \tag{27}$$

The notations ;

$$\begin{aligned} &A_1 = -\tfrac{\alpha}{6},\, A_2 = \tfrac{\beta}{6} \\ &A_3 = \tfrac{\gamma}{3},\, \delta = \tfrac{3}{2}\sqrt{\alpha} \text{ and } \varepsilon = -\tfrac{3}{2}\tfrac{E_0^l}{\sqrt{\alpha}} \end{aligned} \tag{28}$$

Eq. (27) to the form (the sum with λ from 1 to 3) :

$$\begin{aligned} E_{0U} = &\ \theta' \alpha L_U \left(l,\, j,\, s\right)\, a_0^2 A_\lambda A^\lambda \\ E_{0D} = &\ \theta' \beta L_D \left(l,\, j,\, s\right)\, a_0^2 A_\lambda A^\lambda \end{aligned} \tag{29}$$

Where :

$$\begin{aligned} A^1 &= \int_0^{+\infty} \exp\Big(-\delta r^{\frac{4}{3}} - \varepsilon r^{\frac{2}{3}}\Big)\, r^{2l+2-\frac{4}{3}} dr \\ A^2 &= \int_0^{+\infty} \exp\Big(-\delta r^{\frac{4}{3}} - \varepsilon r^{\frac{2}{3}}\Big)\, r^{2l+2-\frac{8}{3}} dr \\ A^3 &= \int_0^{+\infty} \exp\Big(-\delta r^{\frac{4}{3}} - \varepsilon r^{\frac{2}{3}}\Big)\, r^{2l+2-\frac{5}{2}} dr \end{aligned} \tag{30}$$

Now, we make the changes; $r^{\frac{4}{3}} = x^2 \Longrightarrow dr = \frac{3}{2} x dx$, then the above equation reduce to the equivalent form :

$$\begin{aligned} A^1 &= \tfrac{3}{2}\int_0^{+\infty} \exp\left(-\delta x^2 - \varepsilon x\right)\, x^{\left(3l+\frac{5}{2}\right)-1} dx \\ A^2 &= \tfrac{3}{2}\int_0^{+\infty} \exp\Big(-\delta r^{\frac{4}{3}} - \varepsilon r^{\frac{2}{3}}\Big)\, x^{\left(3l+\frac{1}{2}\right)-1} dx \\ A^3 &= \tfrac{3}{2}\int_0^{+\infty} \exp\Big(-\delta r^{\frac{4}{3}} - \varepsilon r^{\frac{2}{3}}\Big)\, x^{\left(3l+\frac{3}{4}\right)-1} dx \end{aligned} \tag{31}$$

We use the following form of special integral [32] :

$$\int_0^{+\infty} x^{v-1} \exp\left(-\delta x^2 - \varepsilon x\right)\, dx = (2\varepsilon)^{-\frac{v}{2}} \Gamma(v)\, \exp\left(\frac{\varepsilon^2}{8\delta}\right)\, D_{-v}\left(\frac{\varepsilon}{\sqrt{2\delta}}\right) \tag{32}$$

We obtain :

$$\begin{aligned} A^1 &= \tfrac{3}{2}(2\varepsilon)^{-\frac{v}{2}} \Gamma\left(3l+\tfrac{5}{2}\right)\, \exp\left(\tfrac{\varepsilon^2}{8\delta}\right)\, D_{-\left(3l+\frac{5}{2}\right)}\left(\tfrac{\varepsilon}{\sqrt{2\delta}}\right) \\ A^2 &= \tfrac{3}{2}(2\varepsilon)^{-\frac{v}{2}} \Gamma\left(3l+\tfrac{1}{2}\right)\, \exp\left(\tfrac{\varepsilon^2}{8\delta}\right)\, D_{-\left(3l+\frac{1}{2}\right)}\left(\tfrac{\varepsilon}{\sqrt{2\delta}}\right) \\ A^3 &= \tfrac{3}{2}(2\varepsilon)^{-\frac{v}{2}} \Gamma\left(3l+\tfrac{3}{4}\right)\, \exp\left(\tfrac{\varepsilon^2}{8\delta}\right)\, D_{-\left(3l+\frac{3}{4}\right)}\left(\tfrac{\varepsilon}{\sqrt{2\delta}}\right) \end{aligned} \tag{33}$$

Inserting eq. (33) in (29) we obtain the noncommutative corrections for energy eigenvalue E_{OU} and E_{OD}.

3.3. The noncommutative spectra for $p = 1$ for NRQM (C.F.P.S.) potential

Now, the non-commutative first-order (in θ) modification of the energy levels E_{1U} and E_{1D}, associated with spin up and spin down, respectively, corresponding to $p = 1$ excited states, will be determined from Esq. (7), (18) and (25) :

$$
\begin{aligned}
E_{1U} = &\ \alpha'\alpha L_U\left(l,\, j=l+\tfrac{1}{2},\, s\right)\int_0^{+\infty}\left[\exp\left(-\tfrac{3}{4}\sqrt{\alpha}r^{\frac{4}{3}}+\tfrac{3}{4}\tfrac{E_1^l}{\sqrt{\alpha}}r^{\frac{2}{3}}\right)\, r^l\left(a_0+a_1r^{\frac{2}{3}}\right)\right]^2 g\left(r\right)\, r^2dr\\
E_{1D} = &\ \alpha'\beta L_D\left(l,\, j=l-\tfrac{1}{2},\, s\right)\int_0^{+\infty}\left[\exp\left(-\tfrac{3}{4}\sqrt{\alpha}r^{\frac{4}{3}}+\tfrac{3}{4}\tfrac{E_1^l}{\sqrt{\alpha}}r^{\frac{2}{3}}\right)\, r^l\left(a_0+a_1r^{\frac{2}{3}}\right)\right]^2 g\left(r\right)\, r^2dr
\end{aligned}
\tag{34}
$$

The above relations can be simplified to the following forms :

$$
\begin{aligned}
E_{1U} = &\ \alpha' L_U\left(l,\, j=l+\tfrac{1}{2},\, s\right)\int_0^{+\infty}\exp\left(-\delta r^{\frac{4}{3}}-\varepsilon r^{\frac{2}{3}}\right)\left(\begin{array}{c} B_1r^{2l+\frac{2}{3}}+B_2r^{2l-\frac{2}{3}}+B_3r^{2l+\frac{1}{6}}\\ B_4r^{2l+2}+B_5r^{2l+\frac{2}{3}}+B_6r^{2l+\frac{5}{6}}\\ B_7r^{2l+\frac{4}{3}}+B_8r^{2l-\frac{2}{3}}+B_9r^{2l+\frac{1}{6}}\end{array}\right)dr\\
E_{1D} = &\ \alpha' L_D\left(l,\, j=l-\tfrac{1}{2},\, s\right)\int_0^{+\infty}\exp\left(-\delta r^{\frac{4}{3}}-\varepsilon r^{\frac{2}{3}}\right)\left(\begin{array}{c} B_1r^{2l+\frac{2}{3}}+B_2r^{2l-\frac{2}{3}}+B_3r^{2l\frac{1}{6}}\\ B_4r^{2l+2}+B_5r^{2l+\frac{2}{3}}+B_6r^{2l+\frac{5}{6}}\\ B_7r^{2l+\frac{4}{3}}+B_8r^{2l-\frac{2}{3}}+B_9r^{2l+\frac{1}{6}}\end{array}\right)dr
\end{aligned}
\tag{35}
$$

Where the covariant notations B_μ with $(\mu=\overline{1,9})$ are determined from the relations :

$$
\begin{array}{lll}
B_1=-\frac{\alpha a_0^2}{6} & B_2=\frac{\beta a_0^2}{6} & B_3=\frac{2a_0a_1\gamma}{3}\\
B_4=-\frac{\alpha a_1^2}{6} & B_5=\frac{\beta a_1^2}{6} & B_6=\frac{\gamma a_1^2}{3}\\
B_7=-\frac{\alpha a_0a_1}{3} & B_8=\frac{a_0a_1\beta}{3} & \text{and } B_9=\frac{2a_0a_1\gamma}{3}
\end{array}
\tag{36}
$$

If we use the contra variant notations B^μ with $(\mu=\overline{1,9})$:

$$
\begin{array}{ll}
B^1=\displaystyle\int_0^{+\infty}\exp\left(-\delta r^{\frac{4}{3}}-\varepsilon r^{\frac{2}{3}}\right)\, r^{2l+\frac{2}{3}}dr, & B^2=\displaystyle\int_0^{+\infty}\exp\left(-\delta r^{\frac{4}{3}}-\varepsilon r^{\frac{2}{3}}\right)\, r^{2l-\frac{2}{3}}dr\\
B^3=\displaystyle\int_0^{+\infty}\exp\left(-\delta r^{\frac{4}{3}}-\varepsilon r^{\frac{2}{3}}\right)\, r^{2l+\frac{1}{6}}dr, & B^4=\displaystyle\int_0^{+\infty}\exp\left(-\delta r^{\frac{4}{3}}-\varepsilon r^{\frac{2}{3}}\right)\, r^{2l+2}dr\\
B^5=\displaystyle\int_0^{+\infty}\exp\left(-\delta r^{\frac{4}{3}}-\varepsilon r^{\frac{2}{3}}\right)\, r^{2l+\frac{2}{3}}dr, & B^6=\displaystyle\int_0^{+\infty}\exp\left(-\delta r^{\frac{4}{3}}-\varepsilon r^{\frac{2}{3}}\right)\, r^{2l+\frac{5}{6}}dr\\
B^7=\displaystyle\int_0^{+\infty}\exp\left(-\delta r^{\frac{4}{3}}-\varepsilon r^{\frac{2}{3}}\right)\, r^{2l+\frac{4}{3}}dr, & B^8=\displaystyle\int_0^{+\infty}\exp\left(-\delta r^{\frac{4}{3}}-\varepsilon r^{\frac{2}{3}}\right)\, r^{2l-\frac{2}{3}}dr\\
\text{and} & B^9=\displaystyle\int_0^{+\infty}\exp\left(-\delta r^{\frac{4}{3}}-\varepsilon r^{\frac{2}{3}}\right)\, r^{2l+\frac{1}{6}}dr
\end{array}
\tag{37}
$$

Now, the same change, the above equation reduces to the equivalent form :

$$
\begin{aligned}
B^1 &= \int_0^{+\infty} \exp\left(-\delta r^{\frac{4}{3}} - \varepsilon r^{\frac{2}{3}}\right) r^{2l+\frac{2}{3}} dr \quad B^2 = \int_0^{+\infty} \exp\left(-\delta r^{\frac{4}{3}} - \varepsilon r^{\frac{2}{3}}\right) r^{2l-\frac{2}{3}} dr \\
B^3 &= \int_0^{+\infty} \exp\left(-\delta r^{\frac{4}{3}} - \varepsilon r^{\frac{2}{3}}\right) r^{2l+\frac{1}{6}} dr \quad B^4 = \int_0^{+\infty} \exp\left(-\delta r^{\frac{4}{3}} - \varepsilon r^{\frac{2}{3}}\right) r^{2l+2} dr \\
B^5 &= \int_0^{+\infty} \exp\left(-\delta r^{\frac{4}{3}} - \varepsilon r^{\frac{2}{3}}\right) r^{2l+\frac{2}{3}} dr \quad B^6 = \int_0^{+\infty} \exp\left(-\delta r^{\frac{4}{3}} - \varepsilon r^{\frac{2}{3}}\right) r^{2l+\frac{5}{6}} dr \\
B^7 &= \int_0^{+\infty} \exp\left(-\delta r^{\frac{4}{3}} - \varepsilon r^{\frac{2}{3}}\right) r^{2l+\frac{4}{3}} dr \quad B^8 = \int_0^{+\infty} \exp\left(-\delta r^{\frac{4}{3}} - \varepsilon r^{\frac{2}{3}}\right) r^{2l-\frac{2}{3}} dr \\
&\text{and} \qquad\qquad B^9 = \int_0^{+\infty} \exp\left(-\delta r^{\frac{4}{3}} - \varepsilon r^{\frac{2}{3}}\right) r^{2l+\frac{1}{6}} dr
\end{aligned}
\tag{38}
$$

The convenient mathematical form :

$$
\begin{aligned}
B^1 &= \tfrac{2}{3}\int_0^{+\infty} \exp\left(-\delta r^{\frac{4}{3}} - \varepsilon r^{\frac{2}{3}}\right) x^{\left(l+\frac{11}{6}\right)-1} dx \quad B^2 = \tfrac{2}{3}\int_0^{+\infty} \exp\left(-\delta r^{\frac{4}{3}} - \varepsilon r^{\frac{2}{3}}\right) x^{\left(l+\frac{4}{3}\right)-1} dx \\
B^3 &= \tfrac{2}{3}\int_0^{+\infty} \exp\left(-\delta r^{\frac{4}{3}} - \varepsilon r^{\frac{2}{3}}\right) x^{\left(3l+\frac{19}{2}\right)-1} dx \quad B^4 = \tfrac{2}{3}\int_0^{+\infty} \exp\left(-\delta r^{\frac{4}{3}} - \varepsilon r^{\frac{2}{3}}\right) x^{\left(3l+\frac{5}{2}\right)-1} dx \\
B^5 &= \tfrac{2}{3}\int_0^{+\infty} \exp\left(-\delta r^{\frac{4}{3}} - \varepsilon r^{\frac{2}{3}}\right) x^{3l+\frac{15}{4}} dx \quad B^6 = \tfrac{2}{3}\int_0^{+\infty} \exp\left(-\delta r^{\frac{4}{3}} - \varepsilon r^{\frac{2}{3}}\right) r^{\left(3l+\frac{7}{4}\right)-1} dx \\
B^7 &= \tfrac{2}{3}\int_0^{+\infty} \exp\left(-\delta r - \varepsilon r^{\frac{2}{3}}\right) r^{\left(3l+\frac{7}{2}\right)-1} dx \quad B^8 = \tfrac{2}{3}\int_0^{+\infty} \exp\left(-\delta r^{\frac{4}{3}} - \varepsilon r^{\frac{2}{3}}\right) r^{\left(3l+\frac{1}{6}\right)-1} dx \\
&\text{and} \qquad\qquad B^9 = \tfrac{2}{3}\int_0^{+\infty} \exp\left(-\delta r^{\frac{4}{3}} - \varepsilon r^{\frac{2}{3}}\right) r^{\left(3l+\frac{19}{12}\right)-1} dx
\end{aligned}
\tag{39}
$$

The above special integral, after a straightforward calculation :

$$\begin{aligned}
B^1 &= \tfrac{2}{3}(2\varepsilon)^{-\frac{v}{2}}\Gamma\left(l+\tfrac{11}{6}\right)\exp\left(\tfrac{\varepsilon^2}{8\delta}\right)D_{-\left(l+\frac{11}{6}\right)}\left(\tfrac{\varepsilon}{\sqrt{2\delta}}\right)\\
B^2 &= \tfrac{2}{3}(2\varepsilon)^{-\frac{v}{2}}\Gamma\left(l+\tfrac{4}{3}\right)\exp\left(\tfrac{\varepsilon^2}{8\delta}\right)D_{-\left(l+\frac{4}{3}\right)}\left(\tfrac{\varepsilon}{\sqrt{2\delta}}\right)\\
B^3 &= \tfrac{2}{3}(2\varepsilon)^{-\frac{v}{2}}\Gamma\left(3l+\tfrac{19}{2}\right)\exp\left(\tfrac{\varepsilon^2}{8\delta}\right)D_{-\left(3l+\frac{19}{2}\right)}\left(\tfrac{\varepsilon}{\sqrt{2\delta}}\right)\\
B^4 &= \tfrac{2}{3}(2\varepsilon)^{-\frac{v}{2}}\Gamma\left(3l+\tfrac{5}{2}\right)\exp\left(\tfrac{\varepsilon^2}{8\delta}\right)D_{-\left(3l+\frac{5}{2}\right)}\left(\tfrac{\varepsilon}{\sqrt{2\delta}}\right)\\
B^5 &= \tfrac{2}{3}(2\varepsilon)^{-\frac{v}{2}}\Gamma\left(3l+\tfrac{15}{4}\right)\exp\left(\tfrac{\varepsilon^2}{8\delta}\right)D_{-\left(3l+\frac{15}{4}\right)}\left(\tfrac{\varepsilon}{\sqrt{2\delta}}\right)\\
B^6 &= \tfrac{2}{3}(2\varepsilon)^{-\frac{v}{2}}\Gamma\left(3l+\tfrac{7}{4}\right)\exp\left(\tfrac{\varepsilon^2}{8\delta}\right)D_{-\left(3l+\frac{7}{4}\right)}\left(\tfrac{\varepsilon}{\sqrt{2\delta}}\right)\\
B^7 &= \tfrac{2}{3}(2\varepsilon)^{-\frac{v}{2}}\Gamma\left(3l+\tfrac{7}{2}\right)\exp\left(\tfrac{\varepsilon^2}{8\delta}\right)D_{-\left(3l+\frac{7}{2}\right)}\left(\tfrac{\varepsilon}{\sqrt{2\delta}}\right)\\
B^8 &= \tfrac{2}{3}(2\varepsilon)^{-\frac{v}{2}}\Gamma\left(3l+\tfrac{1}{6}\right)\exp\left(\tfrac{\varepsilon^2}{8\delta}\right)D_{-\left(3l+\frac{1}{6}\right)}\left(\tfrac{\varepsilon}{\sqrt{2\delta}}\right)\\
B^9 &= \tfrac{2}{3}(2\varepsilon)^{-\frac{v}{2}}\Gamma\left(3l+\tfrac{19}{12}\right)\exp\left(\tfrac{\varepsilon^2}{8\delta}\right)D_{-\left(3l+\frac{19}{12}\right)}\left(\tfrac{\varepsilon}{\sqrt{2\delta}}\right)
\end{aligned} \tag{40}$$

Then, the obtained corrections for $p=1$ excited states :

$$\begin{aligned}
E_{1U} &= \alpha' L_U\left(l,\, j,\, s\right)\, B_\mu B^\mu\\
E_{1D} &= \alpha' L_D\left(l,\, j,\, s\right)\, B_\mu B^\mu
\end{aligned} \tag{41}$$

We have used in the above results the Einstein (sum with indies). For, the stationary state, the two values of $L_U\left(l, j=l+\frac{1}{2}, s\right)$ and $L_D\left(l, j=l-\frac{1}{2}, s\right)$ are equal to and one, while the two values in the first excited states are reduced to *one* and (-2), spin up and spin down, respectively. We summarize the obtained results of energies (E_{0U}, E_{0D}, E_{1U} and E_{1D}) associated with spin up and spin down in the first order perturbation of θ, to the stationary state and the first excited states as follows :

$$\begin{aligned}
E_{0U} &= \pm\sqrt{4\alpha}\left\{\left(2l+\tfrac{7}{3}\right)\,\sqrt{\alpha}+\beta\right\}^{\frac{1}{2}}+\theta'\alpha L_U\left(l,\, j,\, s\right)\, a_0^2 A_\lambda A^\lambda\\
E_{0D} &= \pm\sqrt{4\alpha}\left\{\left(2l+\tfrac{7}{3}\right)\,\sqrt{\alpha}+\beta\right\}^{\frac{1}{2}}+\theta'\alpha L_D\left(l,\, j,\, s\right)\, a_0^2 A_\lambda A^\lambda\\
E_{1U} &= \pm\sqrt{4\alpha}\left\{\left(2l+\tfrac{11}{3}\right)\,\sqrt{\alpha}+\beta\right\}^{\frac{1}{2}}+\alpha' L_U\left(l,\, j,\, s\right)\, B_\mu B^\mu\\
E_{1D} &= \pm\sqrt{4\alpha}\left\{\left(2l+\tfrac{11}{3}\right)\,\sqrt{\alpha}+\beta\right\}^{\frac{1}{2}}+\alpha' L_D\left(l,\, j,\, s\right)\, B_\mu B^\mu
\end{aligned} \tag{42}$$

We can write the commutative central fraction power singular Hamiltonian H_{CFPS} and $H_{SO-CFPS}$ the generated new spin-orbital interaction as :

$$\begin{aligned}
H_{CFPS} &= \left[-\tfrac{\Delta}{2m_0}+\alpha r^{\frac{2}{3}}+\beta r^{-\frac{2}{3}}+\gamma r^{-\frac{4}{3}}\right]\, I_{3\times 3}\\
H_{SO-CFPS} &= \theta g(r)\begin{pmatrix} L_U\left(l,\, j=l+\frac{1}{2},\, s\right) & 0 & 0\\ 0 & L_D\left(l,\, j=l-\frac{1}{2},\, s\right) & 0\\ 0 & 0 & 0\end{pmatrix}
\end{aligned} \tag{43}$$

The operator H_{CFPS} represents an electron interacted exactly with the central fraction power singular potential in ordinary commutative space, while the matrix $H_{SO-CFPS}$ is

the spin-orbit interaction. The new levels are characterized by the quantum numbers $(\mathbf{J},\mathbf{I})$ and $s_z = \pm 1/2$, contrary to the old levels (commutative space) which are depended only on quantum number $\mathbf{I}$ and the 3-parameters of central fraction power singular potential (the studied potential) : α, β and γ.

3.4. The modified Zeeman effect for NRQM (C.F.P.S.) potential :

On another hand, we can draw another physical interpretation for the results of the noncommutativity of the spaces for central fraction power singular potential. If we choose the parameter and the vector of a magnetic field as follows [23]

$$\boldsymbol{\theta} = \varepsilon' \mathbf{B} \text{ and } \theta L_z = \varepsilon' \mathbf{JB} - \varepsilon H_Z \tag{44}$$

Where ε' is a real proportionality-constant, H_Z is the usual Zeeman field. Substituting two Eqs. (20) and (22) into eq. (15) leads to the second new NC Hamiltonian H_{NC-2} as :

$$H_{NC-2} = -\frac{\Delta}{2m_0} + V_{CFPS}(r) + H_{mag-cfps} \tag{45}$$

Where the operator $H_{mag-cfps}$ is given by :

$$H_{mag-cfps} = -\varepsilon' g(r)\ H_Z + \varepsilon g(r)\ JB \tag{46}$$

The above operator $H_{mag-cfps}$ represents two physical interactions between the polarized electron and external magnetic field ; the first one is the ordinary Zeeman Effect and the second is the new interaction coupling between the total momentum $\mathbf{J}$ and external magnetic field $\mathbf{B}$. It is easy to see that the classical limit is guaranteed by the condition $(\theta \longrightarrow 0)$ in NC 3D NRQM. The final expression of (NC-3D NRQM) Hamiltonian $H_{NC-CFPS}$ for (C.F.P.S.) potential can be resumed in the diagonal matrix of order 3×3 as :

$$H_{NC-CFPS} = \begin{pmatrix} \theta g(r) L_U\left(l,\, j = l + \frac{1}{2},\, s\right) + H_{CFPS} + H_{mag-cfps} & 0 & 0 \\ 0 & \theta g(r) L_D\left(l,\, j = l - \frac{1}{2},\, s\right) + H_{CFPS} + H_{mag-cfps} & 0 \\ 0 & 0 & H_{CFPS} \end{pmatrix} \tag{47}$$

It's important to notice that, the noncommutative operator of NC Hamiltonians is changed ; the homage's diagonal elements in commutative Hamiltonian are replaced with different elements :

$$(H_{NC-CFPS})_{11} \neq (H_{NC-CFPS})_{22} \neq (H_{NC-CFPS})_{33} \tag{48}$$

Then, the isotropic commutative Hamiltonian will be in non commutative space anisotropic Hamiltonian.

4. Conclusions

We have obtained the modified bound state solutions of the three-dimensional radial Schrödinger equation for central fraction power singular potential in the case of (NC-3D NRQM), the old states are changed radically and replaced by degenerated new states, depending on four quantum numbers $(\mathbf{J}, \mathbf{l})$ and $s_z = \pm 1/2$ corresponding spin up and spin down. The corresponding NC Hamiltonian represented by 3-matrices , H_{CFPS}, $H_{SO-CFPS}$ and $H_{mag-cfps}$: the first represents the interaction of an electron with spin (1/2) in central fraction power singular potential in commutative ordinary space, while the second matrix represents the spin-orbit interaction, the last part of NC Hamiltonians is the interaction between an electron and an external magnetic field.

Acknowledgments :
This work was supported with search laboratory of Physics and Material Chemistry in University of M'sila, Algeria.

REFERENCES

[1] M, Sameer and all, Central European of Physics. CEJP. 5(4), 516-527, 2007.
[2] S, Anjana, Int J Theor Phys. 37, 2055-2065, 1998.
[3] Shi-Hai, D. and Guo-Huo, S., Foundation of Physics Letters. 16, 357-367, 2003.
[4] L, Buragohai. and S. A. Ahmed, Lat. Am. J. Educ. 3, 573-577, 2009.
[5] Shi-Hai D., Int J Theor Phys. 39, 4, 1119-1128, 2000.
[6] Shi-Hai, D. Foundations of physics Letters. 15, 4, 385-395, 2002.
[7] M. Sameer, Chinese journal of physics. 46, 3, 291-306, 2008.
[8] G. R. Khan, Eur. Phys. J. 53, 123-125, 2009.
[9] Snyder, H. S. , Phys. Rev. 71, 38-41,1947.
[10] Chaichian, M. ; Demichev, A. ; Presnajder, P. Nucl. Phys. B567, 360, 2000.
[11] Jacobus, D. T. PhD, Department of Physics, Stellenbosch University, South Africa, 2010.
[12] Deshpande, N. G. , Parama-J. Phys. 60, 189-198, 2003.
[13] E. Edgard. Quantum, 1st ed. ; (Ellipses : Paris, France, 1998).
[14] Wang, J. H., Li, K. and Dulat, S, Chinese Physics C. 32, 10, 803-806, 2008.
[15] Landi, G. An Introduction to Noncommutative Spaces and Their Geometries ; 1st ed. ; Springer : New York, USA, 1997.
[16] T. Filk, Phys. Lett. B376, 53, 1996.
[17] B. Mirza and M. Zarei , Eur. Phys. J. C. 32, 583, 2004.
[18] Y. I. Manin, Math. Phys. 123, 163, 1989.
[19] A. E. F. Djema and H. Smail, Commun. Theor. Phys. 41, 837-844, 2004.
[20] T. Yoneya, Prog. Theor. Phys. 103, 1081, 2000.
[21] B. Mirza and M. Mohadesi, Commun. Theor. Phys. 42, 664-668, 2004.
[22] Y. Yuan, Y ; Li, K. and Chen, C, Chinese Physics C. 34, 543-547, 2010.
[23] Abdelmadjid Maireche, The African Review of Physics. 9 :0025, 185-195, 2014.
[24] Abdelmadjid Maireche, The African Review of Physics. 9 :0060, 479-483, 2014.
[25] Abdelmadjid Maireche, J. Nano- Electron. Phys. 7 No 2, 02003 ,2015.

[26] L. Mezincescu. Star product in quantum mechanics, arXiv :hep-th/0007046v2. 2000.
[27] M. Chaichain, N. M. Sheikh-Jabbari and A. Tureanu. ArXiv : hep-th/0212259. V1 20 Dec 2002.
[28] J. Gamboa , M. Loewe and J. C. Rojas, ArXiv : hep-th/0010220v4. 14 Jun 2001.
[29] Sameer Ikhdair , Ramazan Sever, Journal of Molecular Structure :THEOCHEM. 806, 155-158, 2007.
[30] S. K. Bose, IL NUOVO CIMENTO. 109B, N. 3, 311-314, 1994.
[31] S. K. Bose, IL NUOVO CIMENTO. 109B, N. 11, 1217-1220, 1994.
[32] I. S. Gradshteyn and I. M. Ryzhik, Table of Integrals, Series and Products, 7th. ed. ; (Academic Press : Burlington, MA, USA, 2007).